The development of laser powder bed fused nano-TiC/NiTi superelastic composites with hierarchically heterogeneous microstructure and considerable tensile recoverable strain

Chenglong Ma[1,6,7,*], Qing Ge[2], Luhao Yuan[2], Dongdong Gu[2,*], Donghua Dai[2], Rossitza Setchi[3], Meiping Wu[1,6,7], Yu Liu[1,6,7], Dongya Li[1,6,7], Shuai Ma[4], Xin Peng[1,6,7], Ziyu Fang[5]

[1] Jiangsu Key Laboratory of Advanced Food Manufacturing Equipment & Technology, Wuxi, 214122, PR China

[2] College of Material Science and Technology, Nanjing University of Aeronautics and Astronautics, Nanjing, 210016, PR China

[3] School of Engineering, Cardiff University, CF24 3AA, UK

[4] College of Mechanical Engineering, Chongqing University of Technology, Chongqing, 400054, PR China

[5] Sino-French Engineer School, Nanjing University of Science and Technology, Nanjing, 210094, PR China

[6] Jiangsu Province Engineering Research Center of Micro-Nano Additive and Subtractive Manufacturing, Wuxi, 214122, PR China

[7] School of Mechanical Engineering, Jiangnan University, Wuxi, 214122, PR China

*Corresponding author. E-mail: Chenglong Ma, chenglongma@jiangnan.edu.cn; Dongdong Gu, dongdonggu@nuaa.edu.cn

**Abstract**

In this study, we fabricated the TiC nanoparticles decorated NiTi-based superelastic composites via laser powder bed fusion (LPBF) technology. Different from reactionlessness between TiC and NiTi in the conventional processes, high energy density of laser beam triggered strong diffusion behavior of carbon atoms from TiC nanoparticles and resulted in the precipitation of $TiC_x$ and attendant Ni-rich even Ti-rich intermetallics. Interestingly, these nanoprecipitates distributed along the intricate network of connected dislocations, architecting a novel submicron-scale cellular reinforcement structure and facilitating the formation of a hierarchically heterogeneous microstructure. The migration and distribution of TiC nanoparticles as well as the forming mechanism of the submicron cellular reinforcement structure were then elaborated. The study indicated laser scanning speed had significant influence on the distribution of TiC nanoparticles, the size of cellular structure and the matrix grain orientation. At the optimized parameter, the LPBF-fabricated nano-TiC/NiTi composites exhibited a weak orientation texture along the building direction, finer cellular structure and a considerable steady recoverable strain of 2.3% at a maximum tensile loading of 300 MPa.

**Keywords:** TiC/NiTi superelastic composites, laser powder bed fusion, microstructure, phase transformation behavior, tensile properties

## 1. Introduction

Particulate-reinforced metal matrix composites (PRMMCs) possess numerous advantages over traditional single materials, such as high specific strength, high specific stiffness, good wear resistance and corrosion resistance [1]. Although lots of relative investigations have been reported, the rapidly increasing demands for high-performance PRMMCs in aerospace, automobile, and medical fields make the PRMMCs remain a hot topic. As the primary shape memory material, NiTi shape memory alloys (SMAs) have witnessed wide applications in aerospace smart skins, deployable structures, surgical instruments, and medical implants, due to its unique shape memory effect (SME) and superelastic effect (SE) simultaneously with excellent damping capacities and good biocompatibility [2-4]. Considering the increasingly complex service environment and the strong demands for higher-performance NiTi-based materials, particulate-reinforced NiTi-based composites also have been proposed. Several ceramic reinforcement materials including $Al_2O_3$ [5], SiC [6], TiN [7], $TiB_2$ [8], $ZrW_2O_8$ [9], and TiC [10] have been used to develop the superelastic composites that are of particular interest in industrial applications. Nevertheless, the relative investigations indicate, although higher yield strengths, greater elastic modulus and improved wear resistance are obtained, the functionalities such as superelasticity get restricted significantly. Also, due to the significant difference in the thermophysical properties (i.e., melting point, thermal conductivity, and coefficient of thermal expansion) of NiTi alloys and ceramic reinforcement materials, stress concentration and even interfacial cracks or pores are prone to form during the fabrication of NiTi-based composites. How to realize simultaneous enhancement in the mechanical properties and functionalities or improve the mechanical properties with less influence on the functionalities is still a great challenge.

Another challenge lies in the fabrication of NiTi alloy and its composites. Owing to the high

reactivity and high ductility of NiTi alloys, there exist many difficulties in the processing and

machining of NiTi-based parts [11, 12]. Recently, additive manufacturing (AM) technologies

based on the novel material incremental manufacturing principle have been paid great attention

[13]. Laser powder bed fusion (LPBF) technology, as the mainstream one of metal AM

technologies, has been implemented for the rapid forming of NiTi-based porous structures [14-

16], showing remarkable advantages in manufacturing parts with any complex configurations over

conventional processes. On the other hand, LPBF belongs to a strong nonequilibrium

metallurgical process due to the rapid heating/cooling nature induced by the high energy density

of laser beam, providing possibility for the formation of unique microstructures and resultant

performance breakthroughs. For example, Y.M Wang et al prepared 316L stainless steels by a

LPBF technique [17]. They found the LPBF-fabricated stainless steels exhibited a hierarchically

heterogeneous microstructure with length scales spanning nearly six orders of magnitude.

Resultantly, high strength and ductility were obtained, surpassing that of conventional 316L steels.

Besides, to widen the applicable material scope of LPBF and enhance the physical or chemical

properties of current materials, second phase addition is becoming an important way to develop

high-performance LPBF-fabricated PRMMCs. However, to the best of our knowledge, limited

investigations on the LPBF of NiTi-based composites have been involved.

Among the reported conventional NiTi-based composite systems, TiC is regarded as a preferred

reinforcement for NiTi alloys, due to its inhibition for the formation of R phase [18], little affect

the extent of SME [19], and reactionlessness with NiTi matrix in a large range of compositions

upon sintering [20]. As early as 1990s, D. Dunand et al had systematacially studied the effects of

TiC particles on the transformation behavior, compressive behavior and SME of NiTi alloys [18, 19, 21]. Z. Zhang et al further found the interface between eutectic TiC and B2 was semi-coherent with different orientation relationships dependent on carbon contents in the NiTi alloys [22]. Recently, D. Zhang et al have attempted to prepare the TiC/NiTi composites by laser directed energy deposition [23]. The results indicated that TiC had the capacity to refine the $Ni_4Ti_3$ precipitates, enhance the strength of NiTi and improve the superelasticity. Different from the conventional methods, laser forming is very conducive to the formation of a variety of metastable phases due to high energy density of laser beam [24]. In our previous work [25, 26], we found that $TiC_x$ dendrites instead of original TiC particles were precipitated during the LPBF of Ni-Ti-C ternary system in which the micro-scale TiC particles with a content of as high as 10 wt.% were used, simultaneously with the formation of Ni-rich intermetallics such as $Ni_4Ti_3$ and $Ni_3Ti$. However, the phase transformation behavior and tensile properties of the LPBF-fabricated TiC/NiTi composites have been not yet studied in details. What's more, according to the recent reports on laser additive manufactured PRMMCs [27-29], it seems that finer reinforcement particles with a relatively lower content are more attractive.

Hence, in this work, we fabricated the 1 wt. % TiC nanoparticles decorated NiTi-based composites via LPBF technology. The effects of laser scanning speed on the phase composition, phase transformation temperature, microstructure, and tensile properties of the LPBF-fabricated nano-TiC/NiTi composites were studied. The formation mechanisms of a hierarchical microstructure involving the dispersion of TiC or $TiC_x$ nanoparticles, the precipitation of the in-situ Ni-rich phases and the formation of submicron cellular reinforcement structure were revealed. Furthermore, the effect of the externally added TiC nanoparticles on the tensile superelastic

behavior of the LPBF-fabricated nano-TiC/NiTi composites were discussed.

**2. Materials and methods**

2.1 Raw materials and powder preparation

In this work, the raw powder materials contained the gas-atomized spherical $Ni_{50.6}Ti_{49.4}$ pre-alloyed powder with a particle size of 15-53 μm and 1 wt. % TiC nanoparticles with an average particle size of 50 nm. The nominal composition of the mixed powder could be described as 49.69Ni-49.43Ti-0.88C (at. %), as the blue arrow shown in Fig. 1a. From the perspective of crystallology, TiC belongs to the interstitial compound that crystallizes in the NaCl-type lattice structure, while B2-NiTi belongs to the intermetallic compound that crystallizes in the CsCl-type lattice structure. The lattice constants of B2-NiTi and TiC are 2.998 Å and 4.327 Å, respectively. Theoretically, if the orientation relationship between TiC and B2-NiTi could meet $<001>_p//<001>_{B2}$, a near-coherent interface would be obtained because of a small misfit of 2.056% (Fig. 1b). The mixing of NiTi pre-alloyed powder and TiC nanoparticles was carried out by the ball milling method with the optimized parameters including ball milling speed of 250 r/min, ball milling time of 2 h and ball-to-powder ratio of 2:1. The as-milled powder was shown in Fig. 1c and 1d. It was clearly observed from the EDS mapping results that a relatively homogeneous composition distribution was achieved (Fig. 1e-g).

2.2 LPBF fabrication

Then, we performed the LPBF process based on the as-milled nano-TiC/NiTi composite powder. The LPBF machine possessed a 500W IPG ytterbium fiber laser (IPG Laser GmbH, Germany), an automatic powder spreading device with flexible scraper blade and an inert argon gas circulatory protection system (the oxygen in the forming environment was roughly 500 ppm).

A batch of bulk and tensile specimens were fabricated using the following processing parameters: laser power $P$ of 225, 250, 275 and 300 W, scanning speed $v$ of 800, 1000, 1200 and 1400 mm/s, hatch spacing $h$ of 60 μm, and layer thickness $d$ of 30 μm. The detailed parameters was listed in the table 1. A 37° rotation strategy between the scanning directions of adjacent layers and an island scanning strategy with island size of 1.2 mm× 1.2 mm were applied during the LPBF process (Fig. 1h).
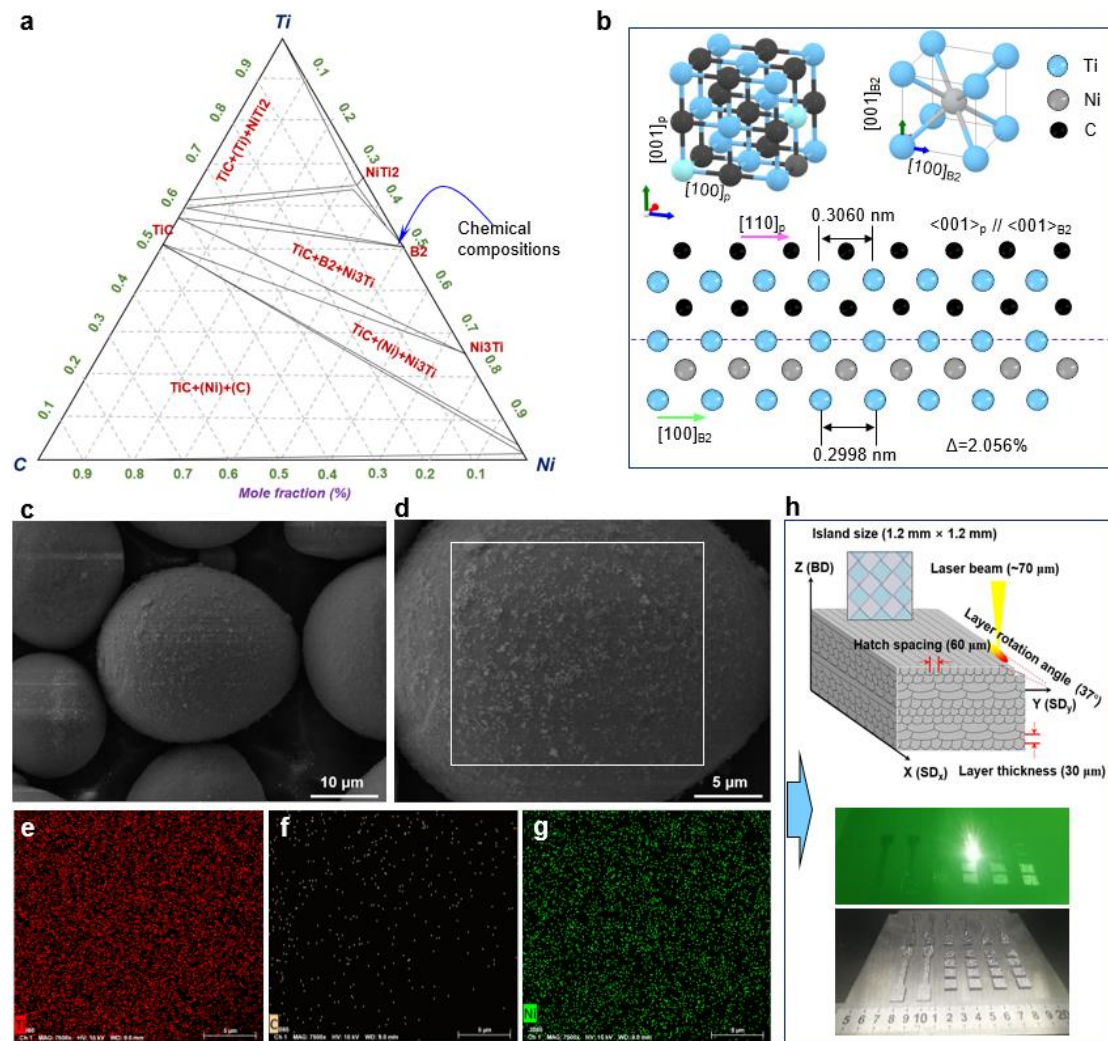


**Fig. 1** The nano-TiC/NiTi-based composite powder developed for the LPBF process. **a** Ti-Ni-C ternary phase diagram; **b** the ideal orientation relationship between TiC lattice and B2 lattice; **c-g** ball-milling prepared NiTi-based composite powder decorated by uniformly dispersed TiC nanoparticles; **h** the LPBF process.

2.3 Microstructure characterization and property tests

The densification behavior of the LPBF-fabricated nano-TiC/NiTi composite samples were firstly evaluated by the Archimedean method and the image method using the optical microscope. Then, four samples with different scanning speed were chosen for the following microstructure characterizations and mechanical tests. The microstructure analysis was performed by a field emission scanning electron microscope (FE-SEM) (ZEISS, Germany) at a voltage of 5 keV. The grain orientation analysis was investigated using electron Backscatter Diffraction (EBSD) performed by a FEI Quanta 650 FEG FESEM (FEI. co., the USA) equipped with HKL Channel 5 system at a voltage of 20 keV. The phases were identified by the Diffraktometer D5000 X-ray diffractometer (XRD) (SIEMENS, Germany) with Cu K radiation (=0.15418 nm) using a continuous scan mode. Also, the transmission electron microscope (TEM) and high resolution TEM (HR-TEM) were carried out by using a Tecnai G2 F20 S-TWIN (operated at 200 kV) (FEI. co., the USA) to analyze the nano-precipitates. Subsequently, tensile experiments were conducted on a CMT5205 testing machine (MTS Industrial Systems, China) in displacement control mode with a cross head velocity of 1 mm/min at room temperature.

**Table 1** The detailed laser processing parameters and corresponding densification degree.

| Sample | Laser power $P$ (W) | Scanning speed $v$ (mm/s) | Line energy density $E$ (J/mm) |
|--------|---------------------|----------------------------|--------------------------------|
| S11 | 225 | 800 | 0.281 |
| S12 | 225 | 1000 | 0.225 |
| S13 | 225 | 1200 | 0.188 |
| S14 | 225 | 1400 | 0.161 |
| S21 | 250 | 800 | 0.313 |
| S22 | 250 | 1000 | 0.250 |
| S23 | 250 | 1200 | 0.208 |
| S24 | 250 | 1400 | 0.179 |
| S31 | 275 | 800 | 0.344 |

| S32 | 275 | 1000 | 0.275 |
| S33 | 275 | 1200 | 0.229 |
| S34 | 275 | 1400 | 0.196 |
| S41 | 300 | 800 | 0.375 |
| S42 | 300 | 1000 | 0.300 |
| S43 | 300 | 1200 | 0.250 |
| S44 | 300 | 1400 | 0.214 |

2.4 Numerical simulation

To better understand the migration behavior of TiC nanoparticles within the molten pool, a simple powder bed model only consisting of two NiTi powder particles decorated by many fine TiC particles was proposed. In consideration of the calculation time cost, the average particle size of TiC phase was magnified three times (namely ~150 nm) in the model. The positions of these TiC particles on the NiTi powder surface were generated based on the random function. Some necessary assumptions were proposed in order to make the problem mathematically tractable, including: (1) the melt at high temperature was considered to be incompressible Newtonian fluid; (2) only melt viscosity, thermal conductivity and surface tension were set as a function of temperature; (3) the surface tension between NiTi melt and TiC particle was set as a constant; (4) the evaporation effect of NiTi melt was ignored. Besides, the other model information including boundary conditions and governing equations could be found in our previous work [30], which were not repeated here.

**3. Results**

3.1 Densification behavior

According to the Archimedean principle, the relative densities of all LPBF-fabricated bulk specimens were measured. Then, we made the process maps to disclose the relationship between laser processing parameters and densification degree (Fig. 2a and 2b). It was shown that the parameter combination of low laser power and high scanning speed tended to induce a relatively

worse densification level (i.e., at $P$=225 W and $v$=1200 mm/s, the specimen exhibited the lowest

densification degree of 97.78%), while the combination of low laser power and low scanning

speed was conducive to the achievement of high densification level (i.e., the highest densification

degree was obtained at $P$=250 W and $v$=800 mm/s, reaching 99.98%). Fig. 2b further depicts the

evolution of densification degree with the line energy density ($E$=$P$/$v$). As the $E$ was increased, the

densification degree generally remained on an upward trend. But there existed a critical value of

about 0.313 J/mm. Once the applied $E$ was larger than 0.313 J/mm, the densification degree

sharply declined. Fig. 2c shows the cross-sectional optical image at a low $E$ of 0.188 J/mm. A

slender and irregular pore was observed in this case, located in the boundary of two types of

molten pools with various orientations. According to the morphology features of the molten pools,

it could be deduced that the pore was formed at the overlap zone between adjacent islands due to

the insufficient energy input. Besides, some spherical pores were also observed, which might

originate from the moisture or hollow particles in the raw powder [31]. As the $E$ was elevated, the

metallurgical defects could get eliminated to a large extent (Fig. 2d). However, when an excessive

$E$ was applied, more spherical pores with a diameter of ~10 μm emerged in the as-fabricated

specimen, as shown in Fig. 2e, which might be attributed to the keyhole dominant fusion mode or

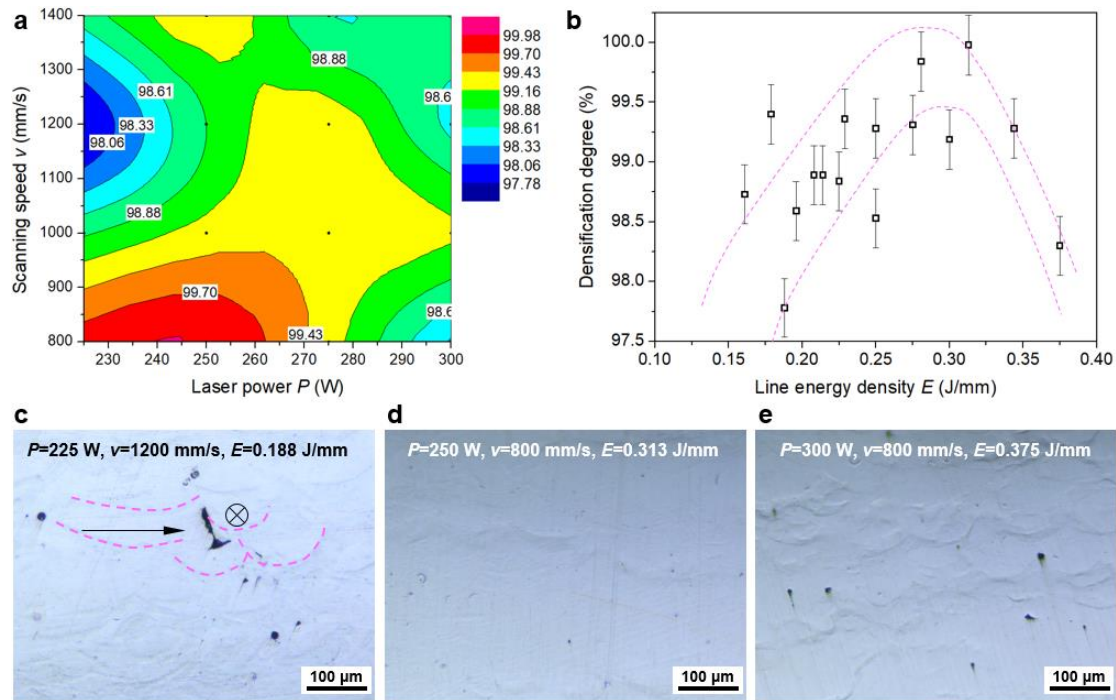the considerable Ni evaporation phenomenon [32].

**Fig. 2** Metallurgical defect analysis of the LPBF-fabricated nano-TiC/NiTi composites. **a** Process parameter map aiming to the densification degree; **b** the evolution of densification degree at different line energy density ($E$); **c-e** cross-sectional optical micrographs of the specimens processed at three typical parameters.

3.2 Phase transformation behavior and tensile properties

Based on the analyses of the densification behavior at different process parameter combinations, we subsequently focused on the variable of scanning speed $v$ and its effects on the phase transformation behavior and mechanical responses of the LPBF-fabricated nano-TiC/NiTi composites. Fig. 3 displays the DSC curves and the thermal hysteresis including $A_f$-$M_s$ and $A_s$-$M_f$ at different $v$ (the laser power was fixed as 250 W). The detailed characteristic transformation temperatures (TTs containing $M_s$, $M_p$, $M_f$, $A_s$, $A_p$, and $A_f$) and enthalpies ($Q_c$ and $Q_h$) were listed in table 2. Overall, all of the DSC curves showed a single transformation peak, indicating the single transformation path B2→B19' in all samples (Fig. 3a). As for the S21 sample with the lowest $v$ of 800 mm/s, the $M_s$ was only 33.1°C, near the ambient temperature, and the $A_s$ was as low as -

10.6°C, which meant the B2 phase dominated in the solidified microstructure. As the $v$ got

increased, both the TTs and the enthalpies significantly shifted to the higher value, contrary to the

reported results in others' investigations [33-35] on the phase transformation behavior of the

LPBF-fabricated NiTi alloys. In their work, the decreased energy input induced by lowering $v$ was

normally conducive to alleviate the Ni evaporation and result in lower TTs. Besides, it was also

noted that the exothermic peak during cooling exhibited a relatively larger peak area (Fig. 3a and

table 2), in comparison with the endotherm peak during the heating process. This could be

attributed to the irreversible energy dissipation such as friction of the austenite-martensite

interfaces [36] and acoustic emissions [37] during the forward transformation. Also, this

irreversible energy dissipation still resulted in the considerable thermal hysteresis [38]. For

instance, the $A_s$-$M_f$ values of all studied samples were basically more than 40°C (Fig. 3b). Besides,

it was found that the $v$ had less influence on the $A_s$-$M_f$ but significant influence on the $A_f$-$M_s$. When

the $v$ of 1000 mm/s was applied, the $A_f$-$M_s$ reached ~42°C, far higher than ~10°C at the $v$ of 800
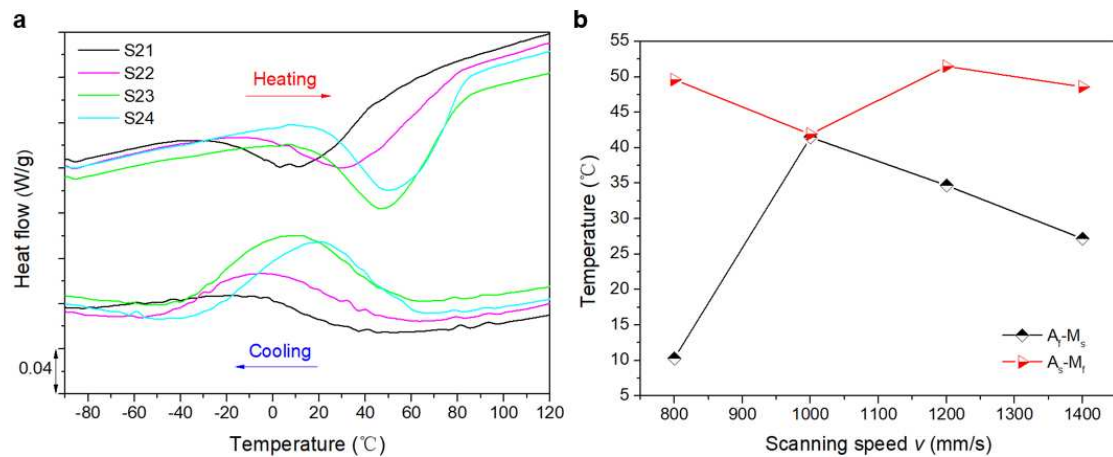
mm/s.



**Fig. 3** Phase transformation behavior of the LPBF-fabricated nano-TiC/NiTi composites at

different $v$. **a** The DSC curves; **b** the thermal hysteresis.

**Table 2** The detailed characteristic transformation temperatures and enthalpies.

| Specimen | Forward transformation | | | | Reverse transformation | | | |
|---|---|---|---|---|---|---|---|---|
| | $M_f$ | $M_p$ | $M_s$ | $Q_c$ | $A_s$ | $A_p$ | $A_f$ | $Q_h$ |
| S21 | -60.2 | -17.2 | 33.1 | 7.686 | -10.6 | 3.1 | 43.4 | -14.29 |
| S22 | -44.4 | -4.7 | 36.8 | 13.73 | -2.5 | 30.0 | 78.3 | -17.94 |
| S23 | -33.2 | 11.6 | 46.8 | 19.86 | 18.3 | 46.8 | 81.5 | -19.79 |
| S24 | -26.3 | 21.2 | 55.7 | 20.15 | 22.3 | 49.9 | 82.9 | -20.3 |

Fig. 4 presents the room temperature tensile mechanical properties of these four LPBF-fabricated nano-TiC/NiTi composite samples. Fig. 4a are the tensile fracture stress-strain curves. It was clearly shown that when the lowest $v$ of 800 mm/s was applied, the largest tensile strength and fracture elongation were obtained, reaching 498.43 MPa and 8.58%, respectively. But with the $v$ increasing, both tensile strength and fracture elongation declined drastically, presenting typical brittle fracture characteristics, which might be mainly associated with the increased porosity. Especially for the pores existing in the overlap zone between adjacent islands, cracks were very prone to occur along the tips of these pores and propagate rapidly under the tensile stress. As for the optimized tensile properties in this study, we further made a comparison with that of the LPBF-fabricated Ni-rich NiTi alloys reported in other work [31, 32, 39, 40], as shown in Fig. 4b. It was found that oxygen content had significant influence on the tensile properties of as-fabricated parts. When the oxygen content was not lower than 500 ppm, our results were apparently superior to others, showing the strengthening effect of TiC nanoparticle. In the future work, strict controls for oxygen content during the powder mixing and LPBF processes need to be implemented to further improve the mechanical properties. Additionally, according to the stress-

strain curves in Fig. 4a, the quasi plateau stress $\sigma_c$ could be estimated by the tangent method. The $\sigma_c$ was roughly 235 MPa for S21 sample and then kept a rising trend as the $v$ was increased. Noticeably, for all samples, the deformation mechanism during the quasi plateau stage should be a mixture of stress-induced martensite transformation (SIMT) and martensite reorientation/detwinning. In views of the difference in transformation temperatures, the SIMT dominated in the deformation mechanism of S21 sample, while martensite reorientation/detwinning induced deformation played an increasing role with the $v$ increasing in other samples.

Furthermore, the cyclic tensile loading-unloading tests were performed to assess the recoverable strain $\varepsilon_{rec}$ at room temperature, as shown in Fig. 4d-h. For the cases in S22-S24, the cyclic tensile responses were similar with a limited hysteresis area and a lower $\varepsilon_{rec}$ (~0.015), showing a quasi linear elastic feature (Fig. 4e-g). But in the case of S21, the sample exhibited a significantly larger hysteresis area with considerable $\varepsilon_{rec}$ and residual strain in the first cycle (Fig. 4d). As the cycle number was increased, the loading-unloading curve gradually became steady and then, the recoverable strain ratio and the $\varepsilon_{rec}$ were plotted with respect to the cycle number in Fig. 4g and 4h. The $\varepsilon_{rec}$ for the first cycle and the 10th cycle in the S21 sample reached 2.75% and 2.26%, respectively, which could match the results of the heat-treated $Ni_{50.4}Ti_{49.6}$ SMA presented in H. Lu et al' s work [41], showing a relatively considerable tensile recovery strain.
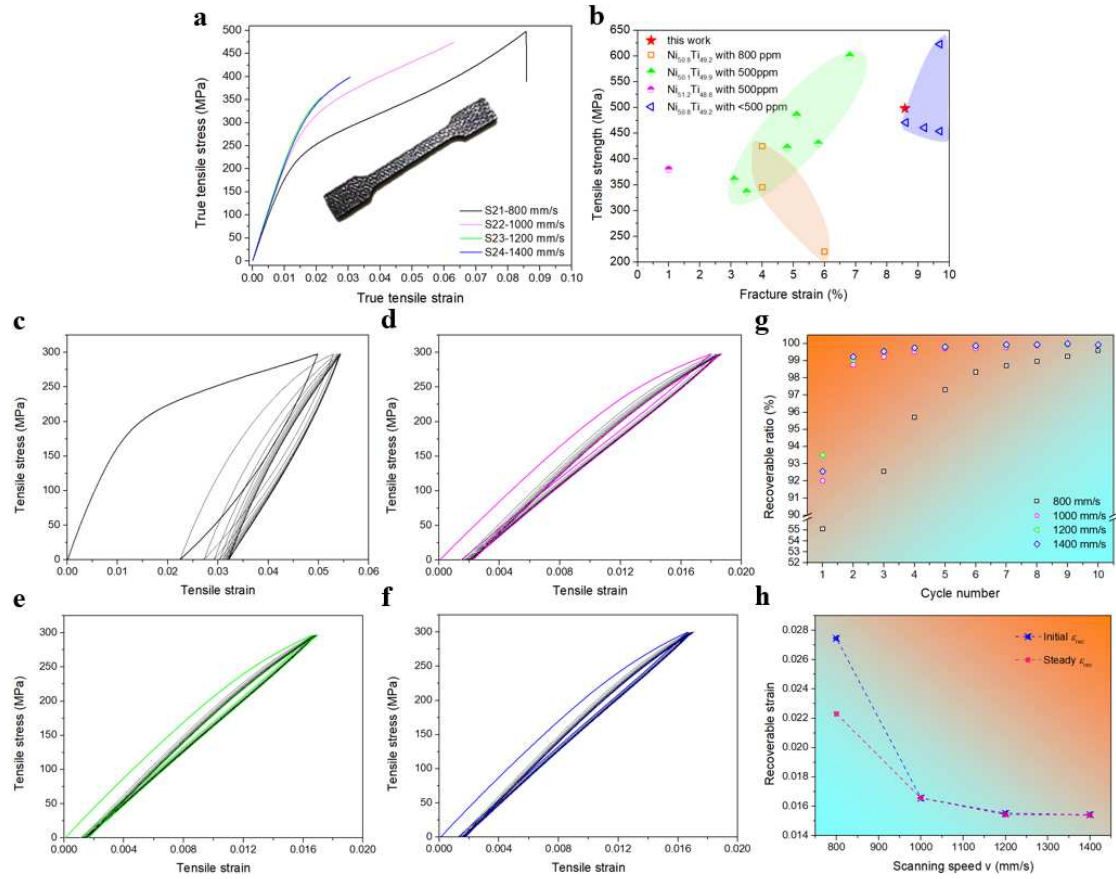
**Fig. 4** Tensile properties and cyclical tensile behavior of the LPBF-fabricated nano-TiC/NiTi

composites at different *v*. **a** Tensile stress-strain curves; **b** comparison with the tensile properties

reported in other work [31, 32, 39, 40]; **c-f** the cyclic tensile stress-strain curves of the samples

fabricated at different *v*; **g** the evolutions of recoverable ratio with cycle number; **h** the recoverable

strain at different *v*.

3.3 Phase characterizations and microstructure features

In view of the considerable difference in phase transformation behavior and tensile mechanical

responses among S21-S24 samples, to reveal the micromechanism behind the difference and the

role of nanoscale TiC particles, the constitutional phases and microstructure features were further

studied in details.

3.3.1 Constitutional phase and phase distribution

Fig. 5a depicts the XRD patterns of the LPBF-fabricated nano-TiC/NiTi composites at different

*v*. It was found that these as-fabricated specimens were mainly composed of B2 phase, B19' phase and TiC phase. A close look at the diffraction peak for $(111)_{TiC}$, which located at $2\theta$ of 37.195° (250 W, 800 mm/s), revealed that the lattice parameter of TiC was *a*=4.183 Å, significantly lower than the standard value of 4.327 Å. This meant TiC phase might exist within the solidified microstructure in a form of substoichiometric $TiC_x$, which had been confirmed by our previous work [25]. As for the dominated phase, the refined results collected within a narrow range of 42.0-45.2° were further given, as shown in Fig. 5b. As relative to the standard diffraction peaks for B2 phase located at the $2\theta$ of 42.801°, the exact position of the $(110)_{B2}$ diffraction peak generally shifted to the higher $2\theta$ angle, with the *v* decreasing from 1400 mm/s to 800 mm/s, indicating a decrease in interplanar distance according to the Bragg's law [42]. It could be deduced that considerable Ni evaporation and carbon atom diffusion occurred during the LPBF of the nano-TiC/NiTi composite when a low *v* was applied. Resultantly, a high concentration of vacancies and interstitial atoms could be produced during the subsequent rapid solidification [43], thereby giving rise to an apparent lattice distortion and attendant decrease in interplanar distance. Fig. 5c demonstrates the evolution of the normalized peak area of $(111)_{B19'}$ relative to $(110)_{B2}$ with the *v*, to roughly reflect the relative volume fraction $f_m$ of retained B19' phase at different *v*. It was clear to be seen that the $f_m$ was apparently elevated by increasing the *v*. What's more, based on three strongest peaks of B2 phase, the modified Williamson-Hall plots of $\sin\theta$ versus $\beta_{hkl}\cdot\cos\theta$ ($\beta_{hkl}$ was the full width at half maximum (FWHM) of the (hkl) diffraction peak) [44] were displayed in Fig. 5d. According to the linear fit to the data, the lattice strain could be estimated from the slope of the fit line. The results implied that high *v* was incline to result in a larger lattice strain.
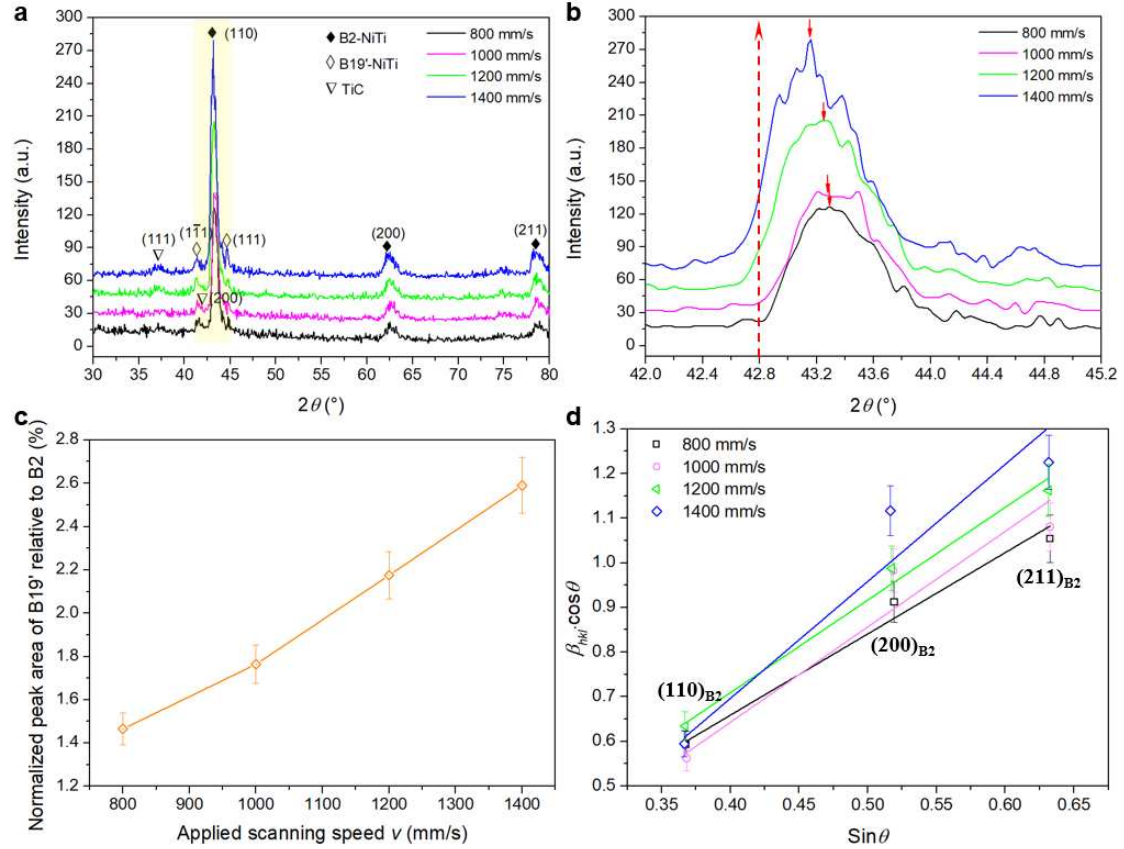
**Fig. 5** Phase analysis of the LPBF-fabricated nano-TiC/NiTi composite. **a** XRD spectra of specimens using different printing parameters; **b** XRD spectra in the vicinity of the standard diffraction peak of B2 phase $2\theta=42.801°$ (as shown the yellow region in **a**); **c** The evolution of normalized peak area with the applied $v$; **d** Modified Williamson-Hall plots for specimens fabricated at different $v$.

The phase distribution in the solidified microstructure was further visualized by the EBSD phase map (Fig. 6). The red, blue and green areas represented the B2 austenite phase, the B19' martensite phase and TiC phase, respectively. Besides, remarkable black area was observed, which mostly distributed along the molten pool boundaries (Fig. 6a), possibly composed of the very fine size of martensite plates and $TiC_x$ precipitates that were out of the ability of the EBSD instrument to catch clear Kikuchi patterns [45]. High $v$ was incline to give rise to more black areas (Fig. 6b-d), which might be closely associated with the serious lattice distortion induced by the increased

residual stress. Besides, the identified martensite phase and TiC phase mostly emerged

surrounding the molten pool boundaries. Also, chain-like TiC particles distributing along the B2

columnar grain boundary were captured in localized region of the S22 sample (Fig. 6b). According

to our previous work [46], prominently higher residual stress produced in the molten pool

boundaries could be responsible for the formation of the large fraction of martensite phase in these
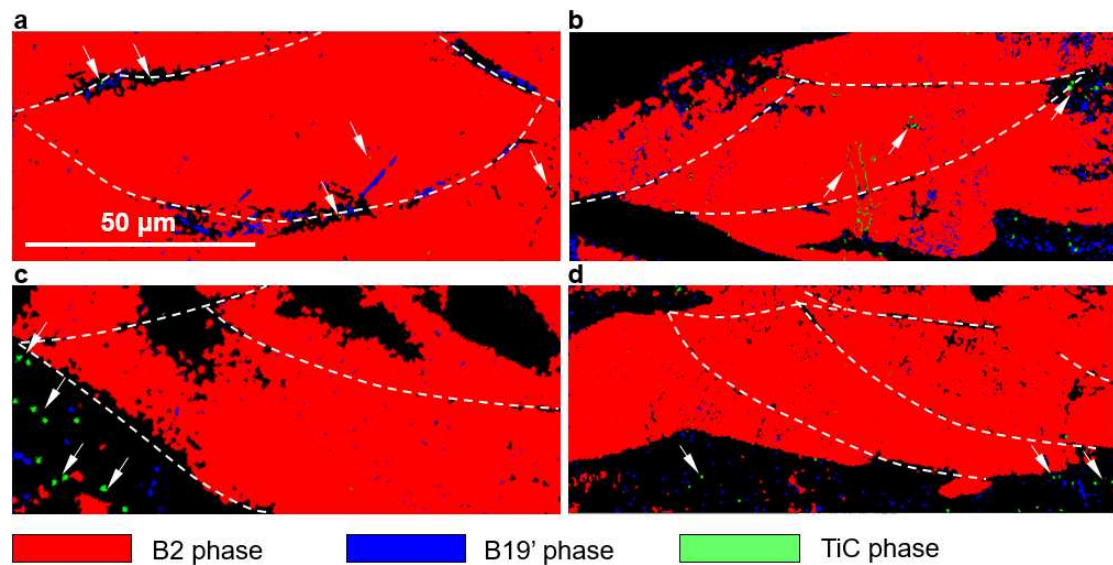
areas.



**Fig. 6** Distribution features of B2, B19' and TiC phases in the cross-sections of the LPBF-

fabricated nano-TiC/NiTi composites at different $v$. **a** $v$=800 mm/s; **b** $v$=1000 mm/s; **c** $v$=1200

mm/s; **d** $v$=1400 mm/s. The white dotted line denoted the molten pool boundary and the white

arrow pointed to the position of the identified TiC phase.

3.3.2 Crystallographic characteristics

Fig. 7 and Fig. 8 show inverse pole figure (IPF) maps and pole figures (PF) obtained by EBSD

analysis of S21-S24 samples, respectively. The relationship between the coordinate system of the

tested sample and the sampling direction was schematized in Fig. 7. The collecting scope for the

acquisition surface was roughly limited in an area only containing a single molten pool. Results

indicated that there hardly existed apparent orientation texture along the building direction (BD) for S21 and S22 samples (Fig. 7a and 7b). While S23 and S24 samples demonstrated strong orientation texture $\{001\}_{B2}$//BD (Fig. 7c and 7d). This could be further confirmed by the PF analysis. First of all, from Fig. 8, all samples showed a considerable maximum texture index $n_{max}>2$ that meant there existed a certain preferred orientation for each sample. When the applied $v$ was 800 mm/s, the $\{111\}_{B2}$ was preferentially oriented about 20° with BD (Fig. 8a). As the $v$ was increased to 1000 mm/s, the preferred orientation could be described as the $\{001\}_{B2}$ oriented about 30° with BD and $X_0Y_0$ plane. When the $v$ was further elevated to 1200 mm/s or 1400 mm/s, the strong orientation texture $\{001\}_{B2}$//BD was observed, as shown in Fig. 8c and 8d. At the $v$ of 1400 mm/s, the $\{001\}_{B2}$ was also preferentially oriented about 30° with $X_0$ axis in $X_0Z_0$ plane. Therefore, it could be concluded that the $v$ remarkably influenced the orientation texture of the LPBF-fabricated nano-TiC/NiTi composites.
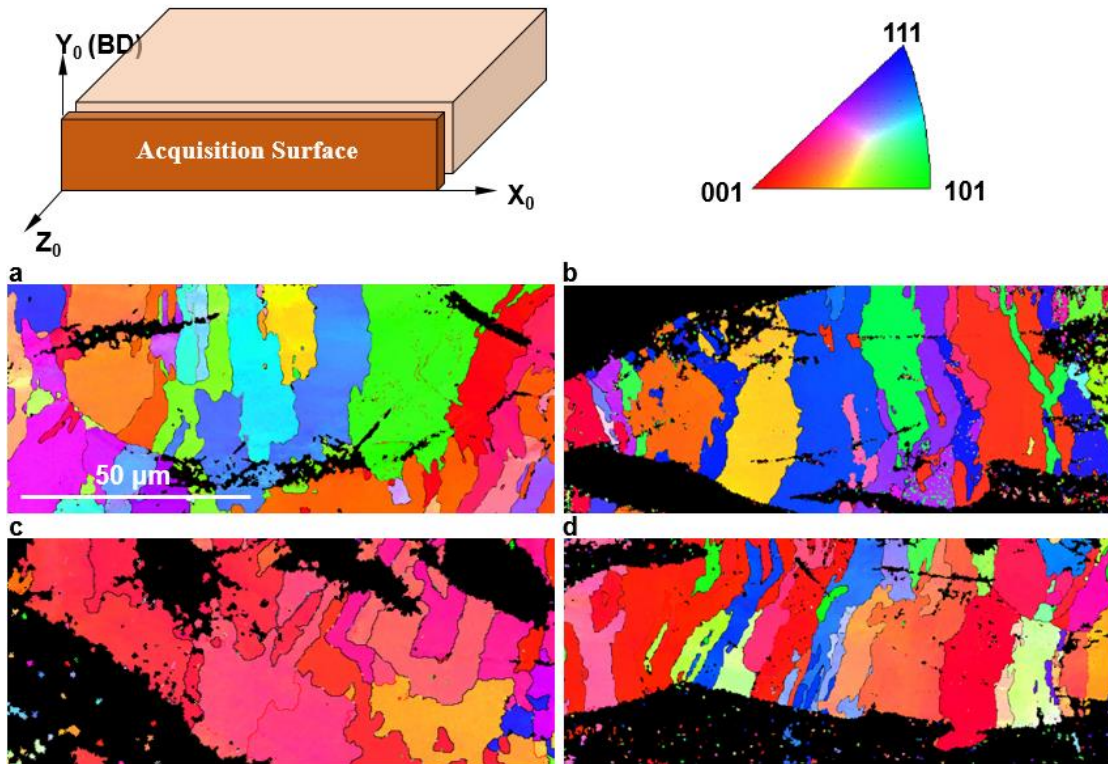


**Fig. 7** The EBSD IPF mapping on the cross sections of the LPBF-fabricated nano-TiC/NiTi

composites at different *v*. **a** *v*=800 mm/s; **b** *v*=1000 mm/s; **c** *v*=1200 mm/s; **d** *v*=1400 mm/s.
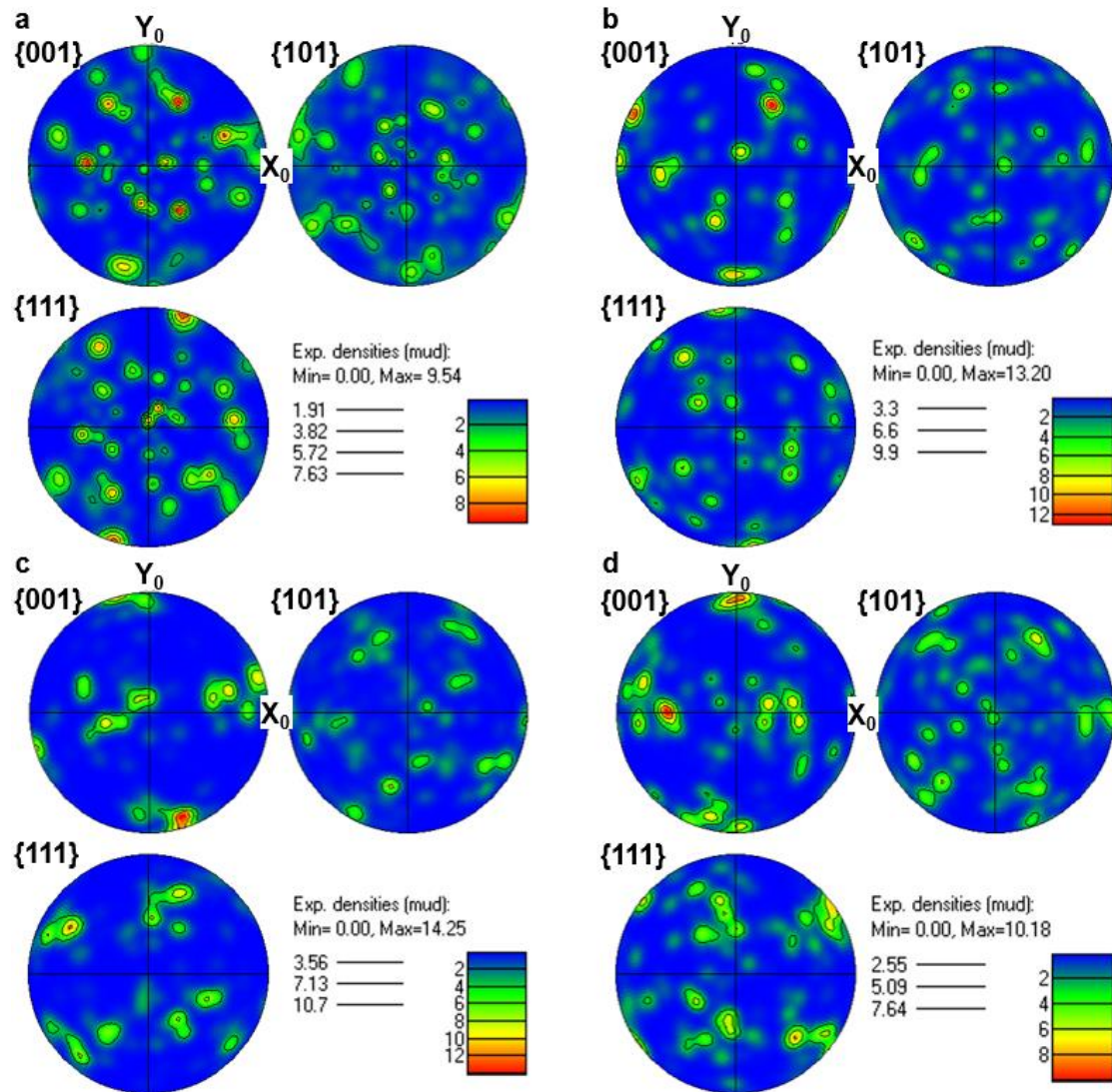


**Fig. 8** The corresponding EBSD PFs of four samples in $\{001\}_{B2}$, $\{101\}_{B2}$ and $\{111\}_{B2}$

orientations. **a** *v*=800 mm/s; **b** *v*=1000 mm/s; **c** *v*=1200 mm/s; **d** *v*=1400 mm/s.

3.3.3 Nanoparticles and nanoprecipitates

Fig. 9 and Fig. 10 show the SEM images of the cross-sectional microstructures of S21-S24

samples. A high density of nanoparticles were observed to be dispersed within the matrix in all

samples. Notably, it was found that more nanoparticles were incline to agglomerate along the

molten pool boundaries (Figs. 9a and 10a). With the applied *v* increasing, the microsegregation got

alleviated to some degree. Besides, an increased *v* also tended to cause the wider molten pool

boundary (Fig. 10). According to the results in Fig. 6, the matrix in the molten pool boundary was

dominated by the B19' phase. Hence, the broadening of the molten pool boundary might be

attributed to an increase in the volume fraction of B19' phase. What's more, in the sample S21, a

great many finer nanoprecipitates were further observed, distributing along the molten pool
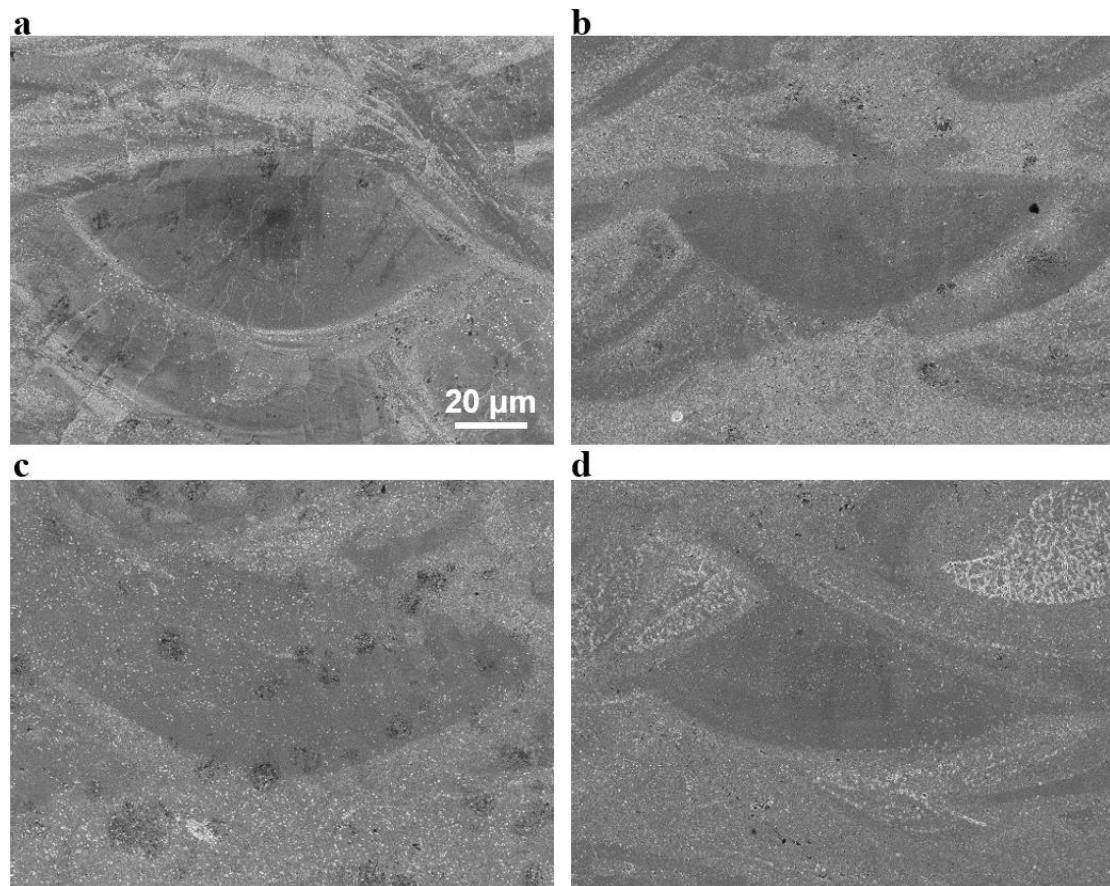
boundary, as the inserted image shown in Fig. 10a.



**Fig. 9** The cross-sectional SEM images of the LPBF-fabricated nano-TiC/NiTi composites at

different $v$. **a** $v$=800 mm/s; **b** $v$=1000 mm/s; **c** $v$=1200 mm/s; **d** $v$=1400 mm/s.
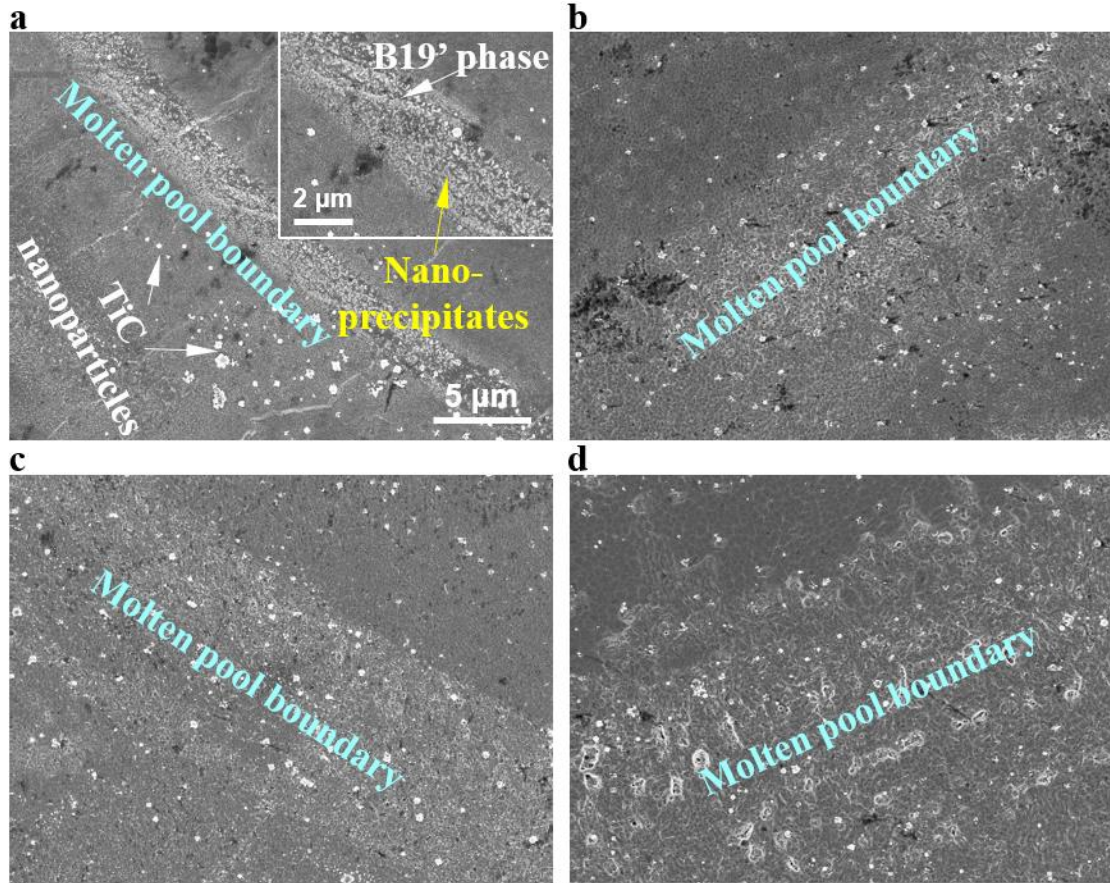
**Fig. 10** The high-magnification SEM images showing the microstructures located at the molten pool boundary. **a** *v*=800 mm/s; **b** *v*=1000 mm/s; **c** *v*=1200 mm/s; **d** *v*=1400 mm/s.

To more clearly identify these nanoprecipitates, the TEM characterizations were performed. Fig. 11a is the TEM microstructure in the vicinity of the molten pool boundary, mainly consisting of strip-like B19' phase and flower-like TiC phase. High-magnification TEM image and the corresponding selected area diffraction pattern (SADP) indicated that the B19' phase contained a plenty of lamellar nano-twins with an orientation relationship of $[-110]_M//[110]_T$ (Fig. 11b and 11c). As for the existed nanoscale TiC phase, apart from the relatively coarsened flower-like dendritic crystals, many granular crystals with an average size of ~100 nm were also found in a strip distribution (Fig. 11d ad 11e). What's more, a large number of precipitates at a much smaller scale (~10nm) distributed in a network or cellular structure (Fig. 11f). Fig. 12 further displays the

HR-TEM images and the corresponding FFT images of the observed granular TiC crystals. By the

EDS analysis, it was found that the crystal A had a relatively higher carbon content than the crystal

B (Fig. 12a and 12d). However, the carbon content of these TiC crystals was far lower than 50

at. %, and the Ti/C atomic ratio ranged from 3 to 6, deviating significantly from the stoichiometric

ratio, which also confirmed the XRD result in 3.3.1 section. Additionally, as for the interface

structure, the A/matrix interface was almost completely coherent (Fig. 12b), while the B crystal

showed an incoherent relationship with the matrix (Fig. 12e). The A/matrix interface was highly

consistent with the ideal condition in Fig. 1b. It seemed that an increase in carbon content was

conducive to obtain a coherent interface.



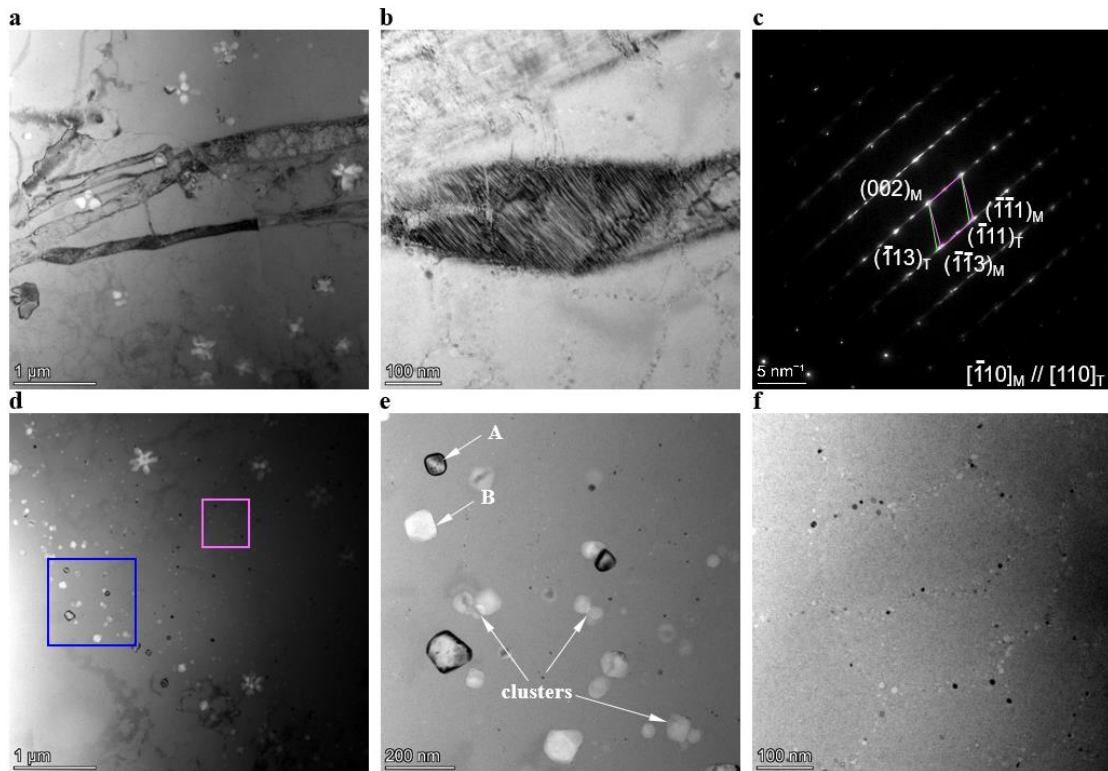**Fig. 11** TEM bright-field images and corresponding SADP of the top-sectional microstructures at

the $v$ of 800 mm/s. **a** Low-magnification morphology of the strip-like B19' phase; **b** local high-

magnification TEM image of **a**; **c** the corresponding SADP of **b**; **d** low-magnification TEM image

showing the segregated $TiC_x$ nanoparticle clusters; **e** high-magnification TEM image in the blue

region of **d**; **f** high-magnification TEM image in the purple region of **d**.
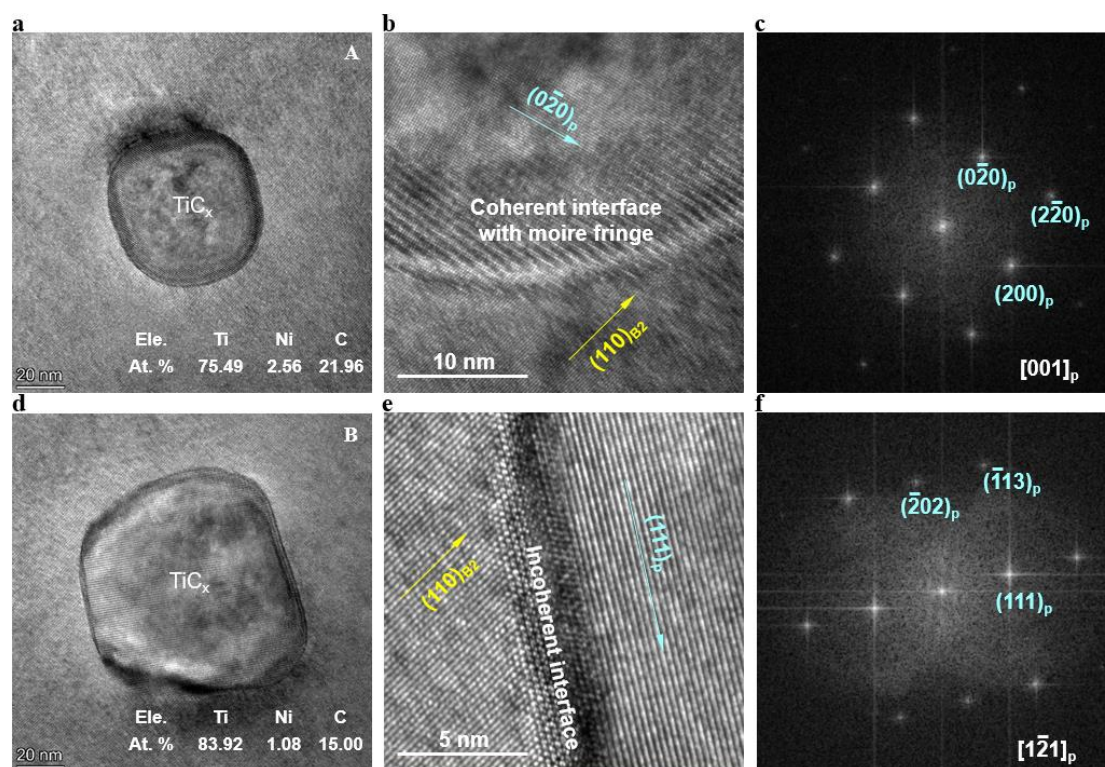


**Fig. 12** High-resolution TEM images and corresponding FFT images of two types of nanoscale TiC$_x$ crystals. **a-c** The crystal A with a carbon content of 21.96 at.%; **d-f** the crystal B with a carbon content of 15.00 at.%.

Apart from the TiC$_x$ nanoparticles, the cellular structure consisting of a variety of nanoprecipitates presented in Fig. 11f was further focused on. Fig. 13a is the high-angle annular dark field (HAADF) TEM image of the cellular structure. By the EDS line analysis, two apparent peaks for Ti element and two valleys for Ni element were observed clearly (Fig. 13b), exactly corresponding to the TiC$_x$ nanoparticles at two ends (Fig. 13a). Additionally, there still existed some relatively weaker constituent fluctuations in the center segment of the line ***mn***. By zooming in further, the sudden changes in Ni and Ti content at the boundaries of the cellular structure were captured, which indicated that the boundaries comprised a certain proportion of Ni-rich intermetallics. Then, we identified these nanoprecipitates emerging at the boundaries based on the

HR-TEM and EDS point analysis. Results showed that the main phase compositions of these

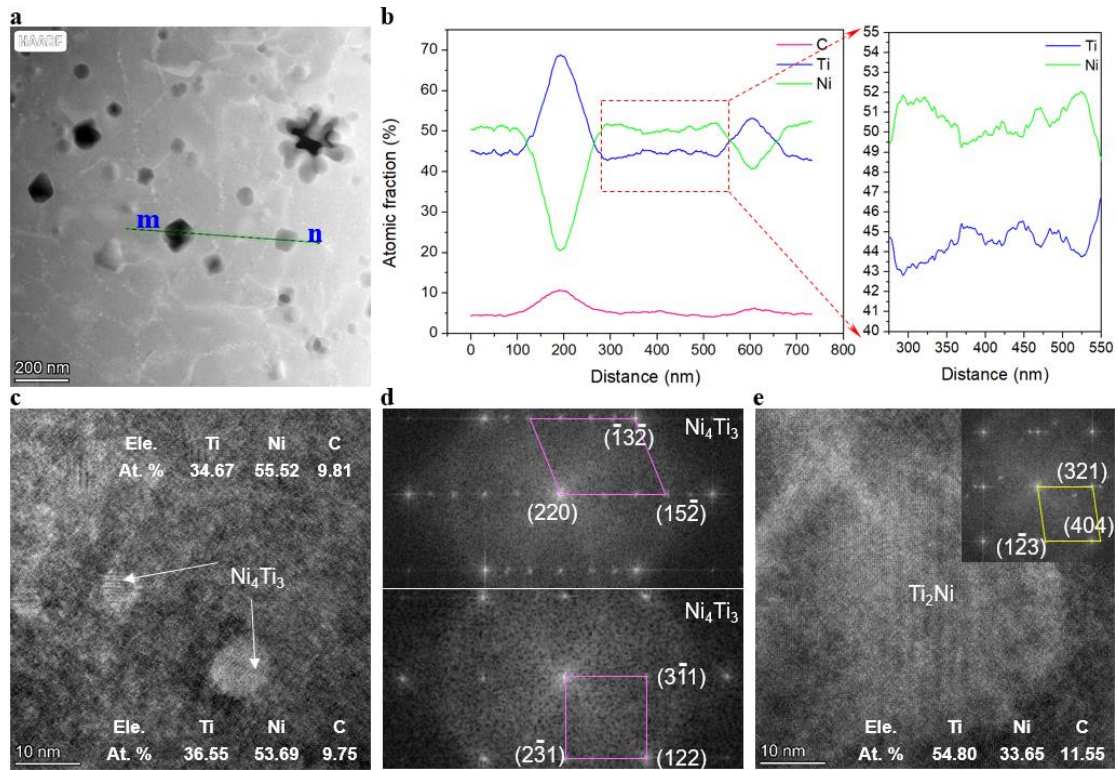nanoprecipitates were $Ni_4Ti_3$ and $Ti_2Ni$, as shown in Fig. 13c-e.



**Fig. 13** The composition analysis and phase identification of the cellular structure. **a** HADDF-

TEM image; **b** EDS line analysis showing the elemental distribution along the line ***mn*** marked in

**a**; **c** HR-TEM image and EDS point analysis showing the morphologies and compositions of the

nanoprecipitates; **d** the corresponding FFT patterns; **e** HR-TEM and the corresponding FFT of

$Ti_2Ni$ nanoprecipitate.

4. Discussion

4.1 Formation mechanism of hierarchically heterogeneous microstructure

According to the EBSD, SEM and TEM characterizations in 3.3 section, a hierarchically

heterogeneous microstructure is formed in the LPBF-fabricated nano-TiC/NiTi composite,

including nanoscale precipitates and dislocations, submicron cellular structures, micron-scale

matrix grains with a certain preferred orientation and mesoscale molten pools. It is believed that

the hierarchically heterogeneous microstructure is the key to the tensile superelasticity with a relatively considerable tensile recovery strain. Obviously, the development of hierarchical microstructure during the solidification is significantly influenced by the distribution of TiC nanoparticles. The diffusion of carbon atoms can result in the change in Ni content of the matrix and facilitate the formation of unique reinforcement structure. Hence, we'll discuss the migration behavior of TiC nanoparticles and precipitation/growth of Ni-rich intermetallics to disclose the formation mechanism of the hierarchically heterogeneous microstructure in the following sections.

4.1.1 Migration and distribution of externally added nanoparticles

Considering that the density $\rho_p$ (4930 kg/m$^3$) of TiC nanoparticle is lower than that $\rho_m$ of NiTi melt (5922 kg/m$^3$), TiC nanoparticle should be not completely insinuated into the static NiTi melt. Fig. 14a and 14b reveal the distribution feature of TiC nanoparticles before and after the interaction between laser beam and composite powders based on the simulation method. As the laser beam moves toward the composite powders, the matrix powders are melt, accompanying with a radially outward flow (Marangoni convection) induced by the large temperature gradient. Then, TiC nanoparticles are migrated along with the flowing melt. Fig. 14c gives the schematic of the dynamics of TiC nanoparticles within the molten pool. For the TiC nanoparticle floating on the melt surface (Fig. 14c$_1$), it mainly suffers from the curvature force $F_r$, effective immersed force $F_{im}$, hydrodynamic drag force $F_D$ and gravity force $G$ [47]. The $F_r$ originates from the Laplace pressure ($P_{sl}=2\gamma_{sl}/R$, where $\gamma_{sl}$ is the interface energy of TiC(nanoparticle)-NiTi(melt) and $R$ is the radius of the nanoparticle) induced by the interface energy and interface curvature, while the $F_{im}$ is caused by the wetting between the nanoparticle and the melt. $F_r$ and $F_{im}$ equal to the integral of the line tension $f_{im}$ and the Laplace pressure $P_{sl}$, respectively. Along the normal direction, a dynamic

equilibrium is reached among the $F_r$, $F_{im}$, and $G$, in views of the strong melt flow. Along the

flowing direction of the melt, TiC nanoparticle will suffer from the $F_D$. The $F_D$ is produced by the

relative motion of TiC nanoparticle and NiTi melt, regarded as the driving force of nanoparticle

migration, given by Stokes' law [48]:

$$F_D = 6\pi\mu_m R v_p \frac{S_m}{4\pi R^2} \tag{1}$$

where $\mu_m$ is the viscosity of the melt, $v_p$ is the relative velocity of TiC nanoparticle relative to the

melt, and $S_m$ is the area of the melt at the nanoparticle surface. Under the action of the $F_D$, TiC

nanoparticles are continuously accelerated until the $v_p$ is decreased to zero. As the distance $d$

between TiC nanoparticles during the migration is reduced significantly, a considerable Van der

Waals force $F_{vdw}$ is therefore generated. The $F_{vdw}$ between two nanoparticles of radii $R$ can be

written as [47]:

$$F_{vdw} = \frac{A_{sys} R^2}{12 R d^2} = \frac{R^2}{12 R d^2} (\sqrt{A_{melt}} - \sqrt{A_{TiC}})^2 \tag{2}$$

where $A_{sys}$, $A_{melt}$ and $A_{TiC}$ are the Hamaker coefficients of the system, NiTi melt and TiC

nanoparticle, respectively. When the $v_p$ is reduced to zero, the $F_{vdw}$ dominates the TiC

nanoparticles to form clusters in the edge of the molten pool. Additionally, as the laser beam

moves away, the solidified front is gradually advanced along the opposite direction of the

nanoparticle motion. Then, these segregated nanoparticles are retained in the molten pool

boundaries, which is verified by the results in Figs. 9a and 10a.

As for the TiC nanoparticle completely submersed into the molten pool, as shown in Fig. 14c$_2$,

it is mainly subjected to the viscous drag force $F_d$ which can be described by:

$$F_d = 6\pi\mu_m R v_p \tag{3}$$

Under the action of the $F_d$, some TiC nanoparticles are migrated into the molten pool center. When

the distance between adjacent nanoparticles reaches small enough, their interactions becomes non-negligible. These interactions mainly contain an attractive force $F_{vdw}$, an energy barrier $W_{barrier}$ preventing the nanoparticles from contacting and sintering, and the Brownian energy $E_b$ promoting the nanoparticles dispersion [49]. The $E_b$ is generated by the random motion of molecules in the molten pool with high temperature, playing a crucial role in the TiC nanoparticles dispersion. The work $W_{vdw}$ of the $F_{vdw}$ between two nanoparticles of radii $R$ can be written as:

$$W_{vdw} = \int_{d_0}^{d} - \frac{R}{12\xi^2}(\sqrt{A_{melt}} - \sqrt{A_{TiC}})^2 d\xi \tag{4}$$

where $d_0$ is the effective action distance of the $F_{vdw}$ (here ~5 nm). The $W_{barrier}$ and $E_b$ can be calculated by the following formula [50, 51]:

$$W_{barrier}(d) = \begin{cases} 2\pi R L(\gamma_{sg} - \gamma_{sl})e^{-(d-L)/a_0} \dfrac{d - a_0}{L - a_0}, & L \le d \le a_0 \\ -2\pi R L \gamma_{sg} e^{d/a_0}(1 - d / L) + 2\pi R L(\gamma_{sg} - \gamma_{sl}), & 0 \le d \le L \end{cases} \tag{5}$$

$$E_b = kT \tag{6}$$

where $L$ is the length of chemical bond, $a_0$ is the characteristic decaying length (normally 0.2~0.4 nm) for the chemical bond, $k$ is the Boltzmann constant and $T$ is the absolute temperature. When $E_b > W_{vdw}$ and $E_b > W_{barrier}$, TiC nanoparticles form clusters in NiTi matrix; When $E_b < W_{vdw}$ and $E_b < W_{barrier}$, TiC nanoparticles form pseudo-dispersion in NiTi matrix; When $E_b > W_{vdw}$ and $E_b < W_{barrier}$, TiC nanoparticles form self-dispersion in NiTi matrix. In this study, we take $A_{melt}$=400 zJ [52], $A_{TiC}$=238 zJ [53], $R$=25 nm, $L$=0.2 nm, $a_0$=0.4 nm to estimate the relationship among these three energies, as shown in Fig. 15. For the TiC nanoparticle with $R \le 5$ nm, they are always able to form self-dispersion. With the $R$ increasing, the critical $d$ to maintain the self-dispersion will get increased continuously. For example, when the $R$=50 nm, the self-dispersion of nanoparticles will hardly occur if the $d$<1.8 nm. This means some nanoparticle clusters might form in the solidified

microstructure, which have been observed in Fig. 11e.

As the laser beam moves away, the molten pool experience a rapid cooling process. In this condition, the $F_{vdw}$ between the solidified front and TiC nanoparticle are also remarkably increased, as shown in Fig. 14c$_2$. Hence, there exists a critical moment when the $F_{vdw}$ is equal to the $F_d$. Then, the TiC nanoparticle will move at a steady $v_s$ which can be described by [54]:

$$v_s = \frac{A_{sys}(d' - 2a_0)}{36\pi R \alpha \mu_m (d' + a_0)^2} \tag{7}$$

where α is the ratio of the thermal conductivity of TiC nanoparticle to NiTi melt. Obviously, the $v_s$ is a function of the distance $d'$ between the solidified front and TiC nanoparticle. By the derivative, the maximum value of the $v_s$ can be estimated, at a scale of $10^{-1} \sim 10^0$ m/s due to the absence of accurate value for $A_{sys}$ and $\mu_m$, roughly close to the solidification rate dependent on the scanning speed $v$. In this case, the agglomeration of TiC nanoparticles along the matrix grain boundaries can occur possibly, as shown in Fig. 6b, which will be able to further guide us to optimize the process parameters and the tensile properties in the future work.
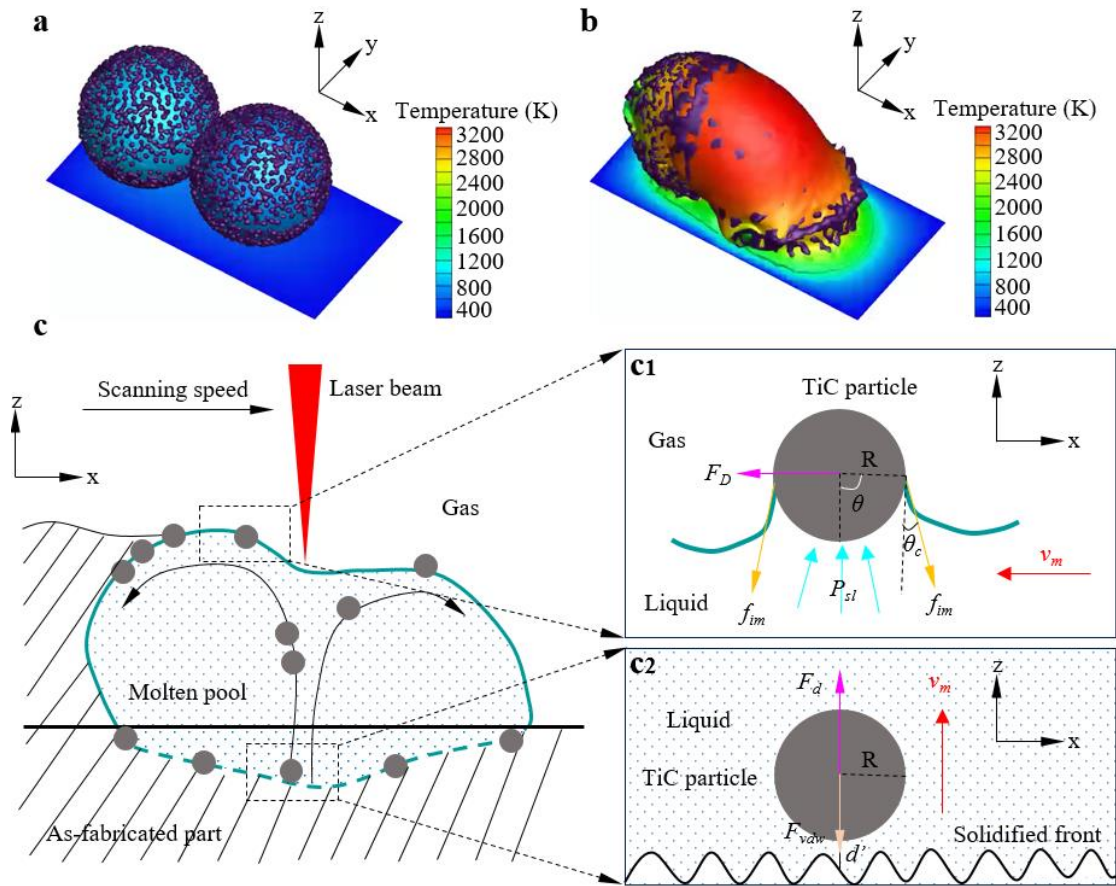
**Fig. 14** The externally added TiC nanoparticle dynamics. **a** and **b** The distribution feature of TiC nanoparticles before and after the laser-powder interaction; **c** schematic diagram of the dominant forces acting on TiC nanoparticles, **c₁** the nanoparticle floating on molten pool surface and **c₂** the nanoparticle completely submerged into molten pool.
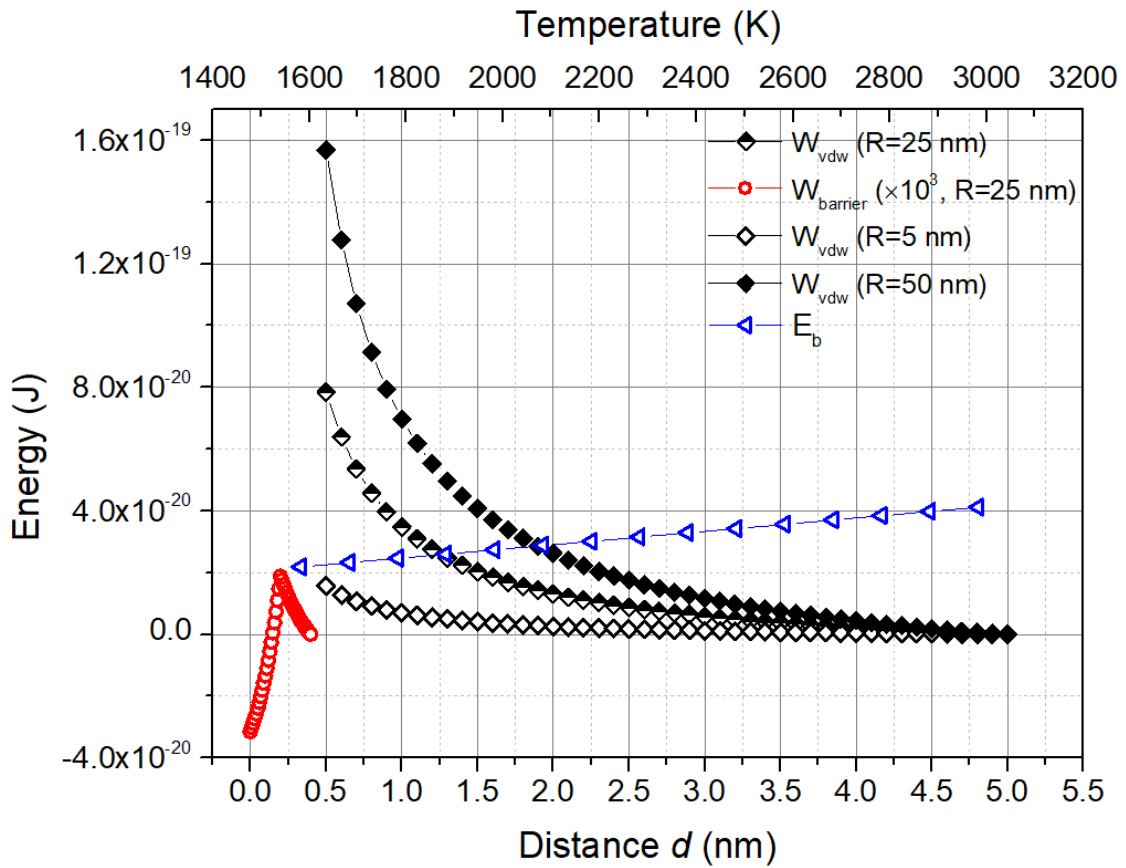
**Fig. 15** The effects of distance between adjacent nanoparticles on $W_{vdw}$ and $W_{barrier}$ and the change of $E_b$ with the operating temperature.

4.1.2 Submicron cellular structure

According to the results presented in Fig. 13, a plenty of fine nanoparticles with an average size of ~8 nm precipitate from the matrix and distribute in a cellular structure. Figs. 16a and b display the STEM images of the cellular structure. A great many dislocation lines with a density of ~$10^9$/cm$^2$ are clearly observed and their distribution is highly consistent with the nanoprecipitate distribution. It has long been known that dislocations can act as nucleation sites of second phases [55], especially for coherent second phases such as Ni$_4$Ti$_3$. From Fig. 13 d-f, we can know that these nanoprecipitates included Ni$_4$Ti$_3$ and Ti$_2$Ni. Besides, it is reasonable to believe that TiC$_x$ nanoparticles also mingle uniformly with these nanoprecipitates, which can be confirmed by the homogeneous element distribution shown in Figs. 16c-f. Figs. 17a and b present the schematic of

the solidification processes and the forming mechanism of the submicron cellular structure. First

of all, during the LPBF processing, the externally added TiC nanoparticles are melt partially, thus

causing considerable carbon atoms diffusing into the molten pool (Fig. 17a-ii). As the molten pool

is rapidly cooled, a large number of nonstoichiometric $TiC_x$ nanoparticles are nucleated firstly

(Fig. 17a-iii). In this condition, Ni atoms are significantly enriched around these $TiC_x$

nanoparticles, therefore facilitating the formation of supersaturated solid solution Ti(Ni) and

supersaturated vacancies under the strong undercooling. Then, by the aggregation and collapse of

vacancies, high density of dislocations form within the matrix (Fig. 17a-iv) [56]. When the laser

beam moves far away, the matrix with excessive Ni concentration is retained. During the

subsequent repeatedly heating stage of LPBF process, dislocations will migrate due to the thermal

motion of supersaturated vacancies and their forming osmotic force [57]. Considering the

dispersed TiC and $TiC_x$ nanoparticles, these dislocations are mostly pinned. On the other hand, due

to the apparent differences in elastic constants (i.g., $C_{44}$) and coefficient of thermal expansion

between the matrix and TiC or $TiC_x$ nanoparticle, considerable thermal mismatch stresses can

form, which further facilitate the multiplication of dislocations. Subsequently, with the cyclic

thermal actions, $Ni_4Ti_3$ precipitates nucleate on these dislocations. According to J. Cahn's work

[55], the critical radius $r_0$ of a $Ni_4Ti_3$ precipitate on an edge dislocation can be calculated by the

minimum in the free energy $F$ per unit length:

$$\frac{\partial F}{\partial r}\bigg|_{r=r_0} = 0$$

$$F = -\frac{Gb^2}{4\pi(1-v)}\ln r + 2\pi\gamma r - \pi\Delta G_v r^2 + C \tag{8}$$

where $G$ is the elastic shear modulus of the matrix (~30 GPa), $b$ is the burgers vector along

$<111>_{B2}$ (0.26 nm), $v$ is the Poisson ratio of the matrix (0.33), $\gamma$ is the interfacial energy of the

Ni$_4$Ti$_3$/B2 boundary (~0.5 J/m$^2$), $\Delta G_v$ is the free energy of unit volume formation of Ni$_4$Ti$_3$ phase

(~-4×10$^9$ J/m$^3$). According to the equation (8), the $r_0$ is 0.11 nm. Then, these Ni$_4$Ti$_3$ nucleuses will

mature and migrate by absorbing abundant solute atoms and vacancies. Simultaneously,

dislocations also climb by the thermal jogs of vacancies. When the dislocation climb speed $v_d$ is

higher than the particle migration speed $v_p$, the unpinning of the dislocations will occur. Hence,

there exists a critical radius $r_c$, the dislocation unpinning will start when $r > r_c$. The $r_c$ can be

estimated by the following equation [58]:

$$\frac{4\pi}{3} r_c^3 = \delta(S - 2r_c)\lambda_e \tag{9}$$

$$\lambda_e = A\exp(F_j / kT) \tag{10}$$

where $\delta$ is the thickness of the Ni$_4$Ti$_3$/matrix interface, $S-2r_c$ is the particle spacing along the

dislocation line, $\lambda_e$ is the equilibrium distance between thermal jogs, A is an atomic distance along

the dislocation line and $F_j$ is the jog activation energy. From Fig. 13, we take $\delta$=0.3 nm, $S$=20 nm,

$A$=0.26 nm, $F_j$=0.4 eV, and $T$=473 K for the equation (9) and (10), and the $r_c$ is calculated as about

8.94 nm. By the TEM observation, the particle radius mainly ranges from 2 nm to 15 nm.

Consequently, part of dislocations can get unpinned, which can be verified by results in Fig. 16a.

Figs. 17c-e shows the effect of laser scanning speed $v$ on the size of the cellular structure. The

mean cell size is apparently enlarged from 150 nm to 363 nm with the $v$ increasing from 800 mm/s

to 1400 mm/s. This variation might mainly originate from the differences in the carbon atom

diffusion behavior and the dislocation density. At a larger $v$ such as 1400 mm/s (Fig. 17e), both the

temperature and life of the molten pool are significantly restricted, resultantly lowering the

diffusion coefficient and diffusion distance of carbon atoms. In this condition, fewer TiC$_x$ particles

and dislocations are formed. Meanwhile, dislocations are more prone to migrate toward grain

boundaries, thus leading to a decrease of dislocation density and an increase of cell size. On the

other hand, weakened carbon diffusion also decreases to some extent the supersaturation of Ni in

the matrix and the fraction of Ni-rich nanoprecipitates during the repeatedly heating stage,

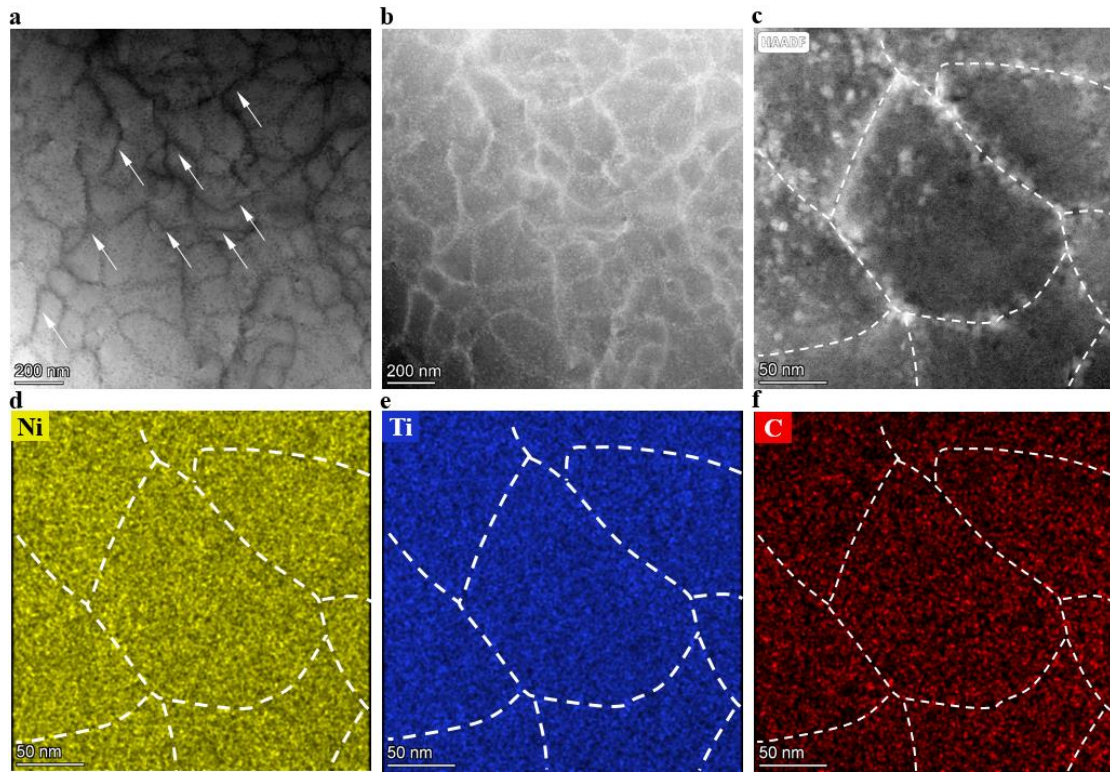accounting for an increase of the transformation temperatures (Fig. 3 and table 2).



**Fig. 16** The morphology feature and element distribution of the cellular structure in S21 sample. **a**

and **b** The bright- and dark-field STEM images; **c** the HAADF image of a single cell; **d-f** the

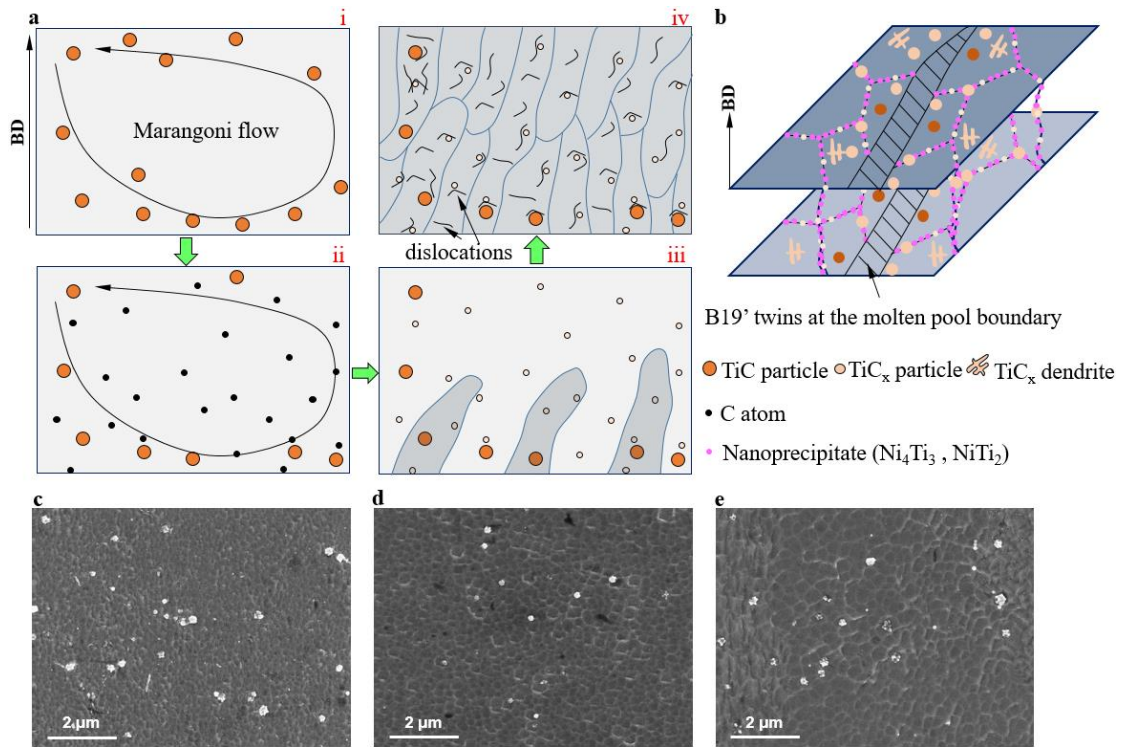distribution of Ni, Ti and C element.

**Fig. 17** The forming mechanism of cellular structure. **a** The schematic of the solidification process; **b** the schematic of the submicron cellular structure; **c-e** SEM images showing the cellular structure obtained at different *v* of 1000, 1200 and 1400 mm/s.

4.2 Effect of TiC nanoparticles on tensile superelasticity of LPBF-fabricated NiTi alloys

The addition of TiC nanoparticles not only facilitates the formation of fine network-distributed nanoprecipitates, but also significantly influences the micro-scale grain orientation and attendant SIMT behavior. In our previous work [46], we found that the as-fabricated NiTi alloy sample always exhibited a very strong texture orientation of $<001>_{B2}$//BD, which was also observed in many others' investigations [31, 32, 34]. But for the S21 sample in this work, the orientation texture of the matrix grain along the BD apparently gets weakened (Figs. 7a and 8a), which can be attributed to the formation of a great many $TiC_x$ nanoparticles that strongly perturb the temperature field of the molten pool [25]. Whereas, as the *v* is increased to 1200 mm/s or 1400 mm/s, a strong orientation texture along the BD is regained (Figs. 7c, 7d, 8c and 8d), due to the

enhanced temperature gradient and a decrease of $TiC_x$ content. Grain orientation can remarkably

affect the transformation stress. According to the previous work [39], the transformation stress in

the as-fabricated NiTi alloys using the similar processing parameters mostly ranges from 350 to

450 MPa, while the value is only ~235 MPa for the S21 sample in this work. Regarding the

martensitic transformation, it is known that B19' martensite is formed by a monoclinic shear

$\{001\}<1-10>_{B2}$ in the B2 matrix, as shown in Fig. 18a. Then, Fig. 18b sketches the relationship

between the $<1-10>_{B2}$ and the tensile direction $F_{tensile}$ in four samples (S21-S24) with different

orientations. For the as-fabricated NiTi alloys or S23 and S24 samples in this work, the angle

between the $<1-10>_{B2}$ and the $F_{tensile}$ is close to 45° due to the strong $<001>_{B2}//BD$ texture. But for

the S21 sample, the angle is reduced to ~20°. Therefore, the resolved shear stress along $<1-10>_{B2}$

in S21 is the largest among these samples, further contributing to the lowest transformation stress

or plateau stress $\sigma_c$. However, in S23 or S24 sample, the $\sigma_c$ is not equal to the transformation

stress, due to more martensite existing in the solidified microstructure (Fig. 5c, Fig. 6c and 6d)

that usually causes a decrease in the $\sigma_c$. Hence, it can be deduced that the B2 phase microstructure

feature still plays a dominated role in determining the value of the $\sigma_c$. The underlying reason might

be associated with the relatively low volume fraction of martensite in the solidified microstructure.

What's more, the S21 sample also exhibits a considerable steady tensile recoverable strain of

~2.3% at a maximum loading of 300 MPa. Obviously, the low $\sigma_c$ is very benefit for the obtainment

of a large recoverable strain. Additionally, the cooperation of dislocations and nanoprecipitates

also plays a vital role. As shown in Fig. 19, the martensitic nanotwin was found along the cellular

structure boundary, formed by the shear of $(110)_{B2}$ with a 15.29° shift. Dislocations and

nanoprecipitates in the matrix can provide sufficient nucleation sites to trigger atomic shearing for

nucleation of martensite. Simultaneously, the submicron-scale cellular structure composed of

dislocations and nanoprecipitates can suppress the dislocation motion during loading and limit

transformation dissipation resulting in a relatively small hysteresis area [59].
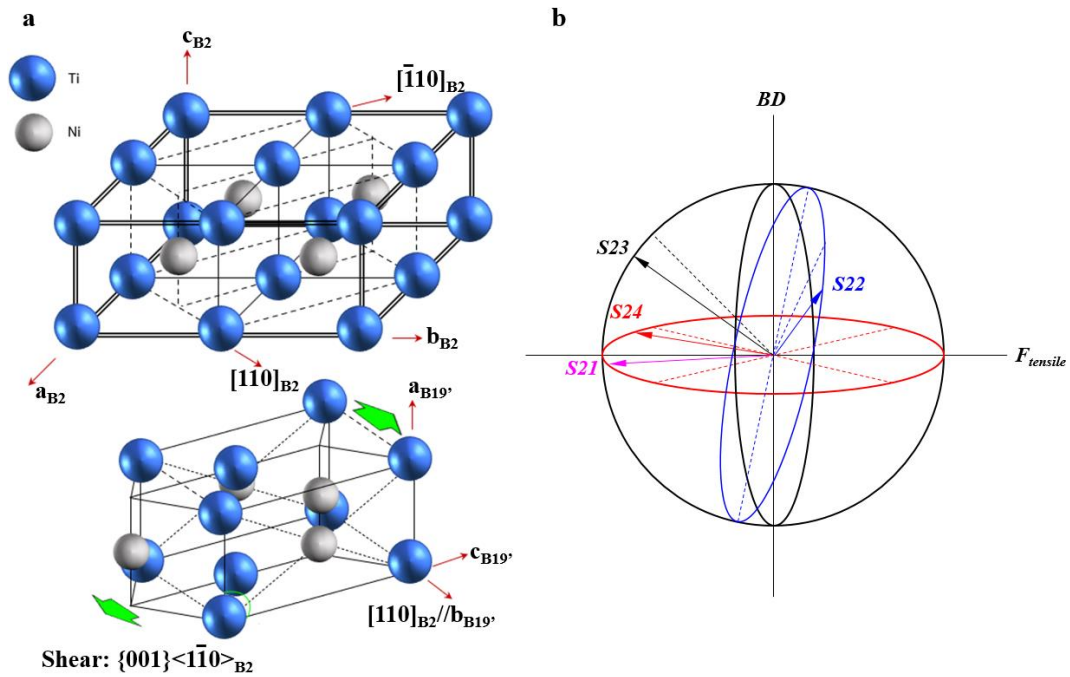


**Fig. 18 a** The schematic of crystal structure relationship between B2 phase and B19' phase; **b** the

schematic of orientation relationship among <1-10>$_{B2}$, tensile direction $F_{tensile}$, and BD.
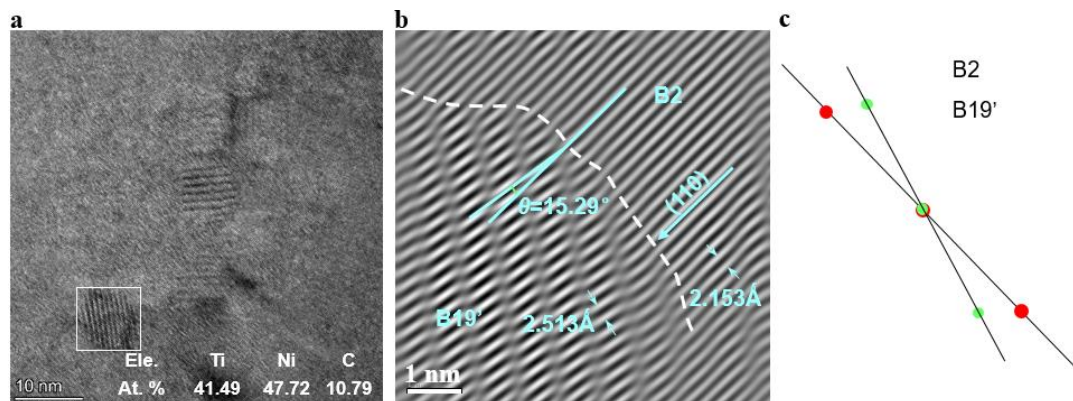


**Fig. 19** TEM analysis of the martensitic nanotwin. **a** HR-TEM image and EDS analysis; **b** inverse

FFT image showing the B2/B19' interface structure; **c** schematic of the corresponding FFT

diffraction spots.

5. Conclusions

In this study, we developed the nano-TiC/NiTi superelastic composites via laser powder bed fusion (LPBF) technology. Some important conclusions could be drawn as follows:

(1) A hierarchically heterogeneous microstructure involving nanoprecipitates, submicron cellular structures, micron matrix grains and mesoscale molten pools was obtained, due to the strong diffusion behavior of carbon atoms from TiC nanoparticles triggered by high energy density of laser beam.

(2) The migration and distribution of TiC nanoparticles were elaborated. The studies indicated that fine TiC nanoparticles with ≤5 nm always could get self-dispersion while the larger TiC nanoparticles tended to form clusters. The laser scanning speed $v$ also influenced the distribution of TiC nanoparticles. By calculation, the maximum velocity of nanoparticles was in a scale of $10^{-1} \sim 10^{0}$ m/s, roughly close to the solidification rate dependent on the $v$. In this condition, a higher $v$ would be able to refrain from the agglomeration of nanoparticles along the grain boundaries.

(3) The submicron cellular reinforcement structure mainly originated from the precipitation of nanoparticles on high density of dislocations during the repeatedly heating stage. With the mature of nanoprecipitates and the climb of dislocations, the dislocation unpinning could occur. The critical radius of the nanoprecipitate was calculated as 8.94 nm, which indirectly got verified by the experimental observations.

(4) Increasing laser scanning speed led to an apparent rise of transformation temperatures, in consideration of its negative effects on the carbon atom diffusion and the supersaturation of Ni in matrix. Besides, with the laser scanning speed increasing, it was also found that the orientation texture along the BD got enhanced and the cellular structure coarsening occurred. This further

gave rise to an increase of the $\sigma_c$ and a decrease of the recoverable strain.

**Acknowledgement**

**Reference**

[1] P. Xiao, Y. Gao, C. Yang, Y. Li, X. Huang, Q. Liu, S. Zhao, F. Xu, M. Gupta. Strengthening and toughening mechanisms of Mg matrix composites reinforced with specific spatial arrangement of in-situ TiB2 nanoparticles. Composites Part B: Engineering, 2020, 198: 108174.

[2] K. Otsuka, X. Ren. Physical metallurgy of Ti–Ni-based shape memory alloys. Progress in Materials Science, 2005, 50: 511–678.

[3] S. Guo, H. Zhang, Y. Chen, Q. Liu, R. Wu, W. Ma, H. Liu, Q. Meng, G. Liu, X. Cheng, X. Zhao. A sandwich-structured Nb/NiTi composite with good bio-compatibility, near-linear-elastic deformation and large elastic admissible strain. Composites Part B: Engineering, 2021, 207: 108586.

[4] S. Liu, S. Han, L. Zhang, L.-Y. Chen, L. Wang, L. Zhang, Y. Tang, J. Liu, H. Tang, L.-C. Zhang. Strengthening mechanism and micropillar analysis of high-strength NiTi–Nb eutectic-type alloy prepared by laser powder bed fusion. Composites Part B: Engineering, 2020, 200: 108358.

[5] M. Farvizi, M.R. Akbarpour, D.-H. Ahn, H.S. Kim. Compressive behavior of NiTi-based composites reinforced with alumina nanoparticles. Journal of Alloys Compounds, 2016, 688: 803-807.

[6] H.J. Jiang, S. Cao, C.B. Ke, X. Ma, X.P. Zhang. Nano-sized SiC particle reinforced NiTi alloy matrix shape memory composite. Materials Letters, 2013, 100: 74-77

[7] Y.C. Luo, D.Y. Li. New wear-resistant material: nano-TiN/TiC/TiNi composite. Journal of Material Science, 2001, 36 (19): 4695-4702.

[8] P.V. Makarov, R.A. Bakeev, A.Y. Peryshkin, A.S. Zhukov, M.K. Ziatdinov, V.V. Promakhov. Modelling of the deformation and destruction of a TiNi-TiB$_2$ metal-ceramic composite fabricated

by direct laser deposition. Engineering Fracture Mechanics, 2019, 222: 106712,

[9] L. Radu, D.Y. Li. Effects of $ZrW_2O_8$ and tungsten additions on the temperature range in which a pseudoelastic TiNi alloy retains its maximum wear resistance. Wear, 2007, 263: 858-865.

[10] R. Vaidyanathan, M.A.M. Bourke, D.C. Dunan. Phase fraction, texture and strain evolution in superelastic NiTi and NiTi–TiC composites investigated by neutron diffraction. Acta Materialia, 1999, 47: 3353-3366.

[11] M. Elahinia. Shape memory alloy actuators: design, fabrication, and experimental evaluation. John Wiley and Sons, Hoboken, New Jersey (2015)

[12] M.H. Elahinia, M. Hashemi, M. Tabesh, S.B. Bhaduri. Manufacturing and processing of NiTi implants: A review. Progress in Materials Science, 2012, 57: 911-946.

[13] L. Ren, Z. Wang, L. Ren, Z. Han, Q. Liu, Z. Song. Graded biological materials and additive manufacturing technologies for producing bioinspired graded materials: An overview. Composites Part B: Engineering, 2022, 242: 110086.

[14] C.L. Ma, D.D. Gu, J. Gao, W. Chen, Y.J. Song, R. Setchi. Mechanical behavior of NiTi-based circular tube chiral structure manufactured by selective laser melting. SDM-2020 7th International Conference on Sustainable Design and Manufacturing, 9-11 September, Split, Croatia.

[15] C.L. Tan, J. Zou, S. Li, P. Jamshidi, A. Abena, A. Forsey, R.J. Moat, K. Essa, M.S. Wang, K.S. Zhou, M.M. Attallah. Additive manufacturing of bio-inspired multi-scale hierarchically strengthened lattice structures. Int. J. Mach. Tools Manuf 167 (2021) 103764.

[16] M. Zhao, H. Qing, Y. Wang, J. Liang, M. Zhao, Y. Geng, J. Liang, B. Lu. Superelastic behaviors of additively manufactured porous NiTi shape memory alloys designed with Menger

sponge-like fractal structures. Materials & Design, 2021, 200: 109448.

[17] Y.M. Wang, T. Voisin, J.T. McKeown, J. Ye, N.P. Calta, Z. Li, Z. Zeng, W. Chen, T.T. Roehling, R.T. Ott, M.K. Santala, P.J. Depond, M.J. Matthews, A.V. Hamza, T. Zhu. Additively manufactured hierarchical stainless steels with high strength and ductility. Nature Materials, 2018, 17: 63-71.

[18] D. Mari, D.C. Dunand. NiTi and NiTi-TiC Composites: Part I. Transformation and Thermal Cycling Behavior. Metallurgical and Materials Transactions A, 1995, 26A: 2833-2847.

[19] K.L. Fukani-Ushhiro, D.C. Dunand. NiTi and NiTi-TiC Composites: Part III. Shape-Memory Recovery. Metallurgical and Materials Transactions A, 1996, 27A: 193-203.

[20] S.N. Kul'kov, T.M. Poletika, A.Y. Chukhlomin, V.E. Panin. Influence of the phase composition of TiC-NiTi composite materials on the character of failure and mechanical properties. Soviet Powder Metallurgy and Metal Ceramics, 1984, 23: 652-655.

[21] K.L. Fukani-Ushhiro, D. Mari, D.C. Dunand. NiTi and NiTi-TiC Composites: Part II. Compressive Mechanical Properties. Metallurgical and Materials Transactions A, 1996, 27A: 183-191.

[22] Z. Zhang, J. Frenzel, C. Somsen, J. Pesicka, K. Neuking, G. Eggeler. Orientation relationship between TiC carbides and B2 phase in as-cast and heat-treated NiTi shape memory alloys. Materials Science and Engineering A., 2006, 438-440: 879-882.

[23] D. Zhang, Y. Li, H. Wang, W. Cong. An Investigation on Ni4Ti3 Phase Precipitation and its Effects in Laser Directed Energy Deposition of TiC-NiTi Composites. Materials Science and Engineering A, 2021, 809: 140976.

[24] T. DebRoy, H.L. Wei, J.S. Zuback, T. Mukherjee, J.W. Elmer, J.O. Milewski, A.M. Beese,

A. Wilson-Heid, A. De, W. Zhang. Additive manufacturing of metallic components – Process, structure and properties. Progress in Materials Science, 2018, 92: 112–224.

[25] C.L. Ma, D.D. Gu, D.H. Dai, G.Q. Yu, M.J. Xia, H.Y. Chen. Thermodynamic behaviour and formation mechanism of novel titanium carbide dendritic crystals within a molten pool of selective laser melting TiC/Ti–Ni composites. CrystEngComm, 2017, 19: 1089-1099;

[26] D.D. Gu, C.L. Ma. In-situ formation of Ni4Ti3 precipitate and its effect on pseudoelasticity in selective laser melting additive manufactured NiTi-based composites. Applied Surface Science, 2018, 441: 862-870;

[27] Q. Han, Y. Gu, J. Huang, L. Wang, K.W.Q. Low, Q. Feng, Y. Yin, R. Setchi. Selective laser melting of Hastelloy X nanocomposite: Effects of TiC reinforcement on crack elimination and strength improvement. Composites Part B: Engineering, 2020, 202: 108442.

[28] C. Guo, Z. Yu, X. Hu, G. Li, F. Zhou, Z. Xu, S. Han, Y. Zhou, R.M. Ward, Q. Zhu. $Y_2O_3$ nanoparticles decorated IN738LC superalloy manufactured by laser powder bed fusion: Cracking inhibition, microstructures and mechanical properties. Composites Part B: Engineering, 2022, 230: 109555.

[29] C.L. Tan, J. Zou, D. Wang, W. Ma, K.S. Zhou. Duplex strengthening via SiC addition and in-situ precipitation in additively manufactured composite materials. Composites Part B: Engineering, 2022, 236: 109820.

[30] Q. Ge, D. Gu, D. Dai, C.L. Ma, Y. Sun, X. Shi, Y. Li, H. Zhang, H. Chen. Mechanisms of laser energy absorption and melting behavior during selective laser melting of titanium-matrix composite: Role of ceramic addition. Journal of Physics D: Applied Physics, 2021, 54: 115103.

[31] L. Xue, K.C. Atli, C. Zhang, N. Hite, A. Srivastava, A.C. Leff, A .A. Wilson, D.J. Sharar, A.

Elwany, R. Arroyave, I. Karaman. Laser Powder Bed Fusion of Defect-Free NiTi Shape Memory Alloy Parts with Superior Tensile Superelasticity. Acta Materialia, 2022, 229: 117781.

[32] L. Xue, K.C. Atli, S. Picak, C. Zhang , B. Zhang, A. Elwany, R. Arroyave, I. Karaman. Controlling martensitic transformation characteristics in defect-free NiTi shape memory alloys fabricated using laser powder bed fusion and a process optimization framework. Acta Materialia, 2021, 215: 117017.

[33] X. Wang, J. Yu, J. Liu, L. Chen, Q. Yang, H. Wei, J. Sun, Z. Wang, Z. Zhang, G. Zhao, J.V. Humbeeck. Effect of process parameters on the phase transformation behavior and tensile properties of NiTi shape memory alloys fabricated by selective laser melting. Additive Manufacturing, 2020, 36: 101545.

[34] S. Saedi, N.S. Moghaddam, A. Amerinatanzi, M. Elahinia, H.E. Karaca. On the effects of selective laser melting process parameters on microstructure and thermomechanical response of Ni-rich NiTi. Acta Materialia, 2018, 144: 552-560.

[35] Y. Yang, J.B. Zhan, Z.Z. Sun, H.L. Wang, J.X. Lin, Y.J. Liu, L.C. Zhang. Evolution of functional properties realized by increasing laser scanning speed for the selective laser melting fabricated NiTi alloy. Journal of Alloys and Compounds, 2019, 804: 220-229.

[36] C. Ma, D. Gu, R. Setchi, D. Dai, M. Wu, S. Ma, X. Miao. A large compressive recoverable strain induced by heterogeneous microstructure in a Ni50.6Ti49.4 shape memory alloy via laser powder bed fusion and subsequent aging treatment. Journal of Alloys and Compounds, 2022, 918: 165620

[37] S. Sreekals, G. Ananthakrishna. Acoustic emission and shape memory effect in the martensitic transformation. Physical Review Letters, 2003, 90: 135501.

[38] H. Sehitoglu, R. Hamilton, H.J. Maier, Y. Chumlyakov. Hysteresis in NiTi alloys. Journal de Physique IV France, 2004, 115: 3–10

[39] M. Nematollahi, S.E. Saghaian, K. Safaei, P. Bayati, P. Bassani, C. Biffi, A. Tuissi, H. Karaca, M. Elahinia. Building orientation-structure-property in laser powder bed fusion of NiTi shape memory alloy. Journal of Alloys and Compounds, 2021, 873: 159791.

[40] N.S. Moghaddam, S.E. Saghaian, A. Amerinatanzi, H. Ibrahim, P. Li, G.P. Toker, H.E. Karaca, M. Elahinia. Anisotropic tensile and actuation properties of NiTi fabricated with selective laser melting. Materials Science and Engineering A, 2018, 724: 220-230.

[41] H.Z. Lu, H.W. Ma, W.S. Cai, X. Luo, Z. Wang, C.H. Song, S. Yin, C. Yang. Stable tensile recovery strain induced by a $Ni_4Ti_3$ nanoprecipitate in a $Ni_{50.4}Ti_{49.6}$ shape memory alloy fabricated via selective laser melting. Acta Materialia, 2021, 219: 117261.

[42] D. Gu, Y.C. Hagedorn, W. Meiners, G. Meng, R. Batista, K. Wissenbach, R. Poprawe. Densification behavior, microstructure evolution, and wear performance of selective laser melting processed commercially pure titanium. Acta Materialia, 2012, 60: 3849–3860.

[43] Q. Zhang, S. Hao, Y. Liu, Z. Xiong, W. Guo, Y. Yang, Y. Ren, L. Cui, L. Ren, Z. Zhang. The microstructure of a selective laser melting (SLM)-fabricated NiTi shape memory alloy with superior tensile property and shape memory recoverability. Applied Materials Today, 2020, 19: 100547.

[44] R.Yogamalar, S. Ramasamy, A. Vinu, K. Ariga, A. Bose. X-ray peak broadening analysis in ZnO nanoparticles. Solid State Communication, 2009, 149: 1919–1923.

[45] X. Wang, M. Speirs, S. Kustov, B. Vrancken, X. Li, J.-P. Kruth, J.V. Humbeeck. Selective laser melting produced layer-structured NiTi shape memory alloys with high damping properties

and Elinvar effect. Scripta Materialia, 2018, 146: 246-250.

[46] D.D. Gu, C.L. Ma, D.H. Dai, J.K. Yang, H.M. Zhang, H. Zhang. Additively Manufacturing Enabled Hierarchical NiTi-based Shape Memory Alloys with High Strength and Toughness. Virtual and Physical Prototyping, 2021, 16: S19-S38.

[47] Y. Zhang, Y. Yu, L. Wang, Y. Li, F. Lin, W. Yan. Dispersion of reinforcing micro-particles in the powder b e d fusion additive manufacturing of metal matrix composites. Acta Materialia, 2022, 235: 118086.

[48] R.B. Bird, W.E. Stewart, E.N. Lightfoot. (2002) Transport Phenomena, Second Edition. John Wiley & Sons, Inc., New York.

[49] P. Jin, Y. Liu, F. Li, Q. Sun. Realization of synergistic enhancement for fracture strength and ductility by adding TiC particles in wire and arc additive manufacturing 2219 aluminium alloy. Composites Part B: Engineering, 2021, 219: 108921.

[50] J.Q. Xu. Achieving Uniform Nanoparticle Dispersion in Metal Matrix Nanocomposites. University of California, Los Angeles, 2015, pp.134.

[51] L.-Y. Chen, J.-Q. Xu, H. Choi, M. Pozuelo, X. Ma, S. Bhowmick, J.-M. Yang, S. Mathaudhu, X.-C. Li, Processing and properties of magnesium containing a dense uniform dispersion of nanoparticles. Nature, 2015, 528 (7583): 539–543.

[52] J.Q. Xu, L.Y. Chen, H. Choi, X.C. Li. Theoretical study and pathways for nanoparticle capture during solidification of metal melt. Journal of Physics: Condensed Matter, 2012, 24: 255304.

[53] R.G. Lye, E.M. Logothetis. Optical Properties and Band Structure of Titanium Carbide. Physics Reviews, 1966, 147: 622-635.

[54] R. Shi, J.M. Meier, A.A. Luo. Controlling Particle/Metal Interactions in Metal Matrix Composites during Solidification: The Role of Melt Viscosity and Cooling Rate. Metallurgical and Materials Transaction A, 2019, 50A: 3736-3747.

[55] J.W. Cahn. Nucleation on dislocations. Acta Metallurgica, 1957, 5: 169-172.

[56] G. Schoeck, W.A. Tiller. On dislocation formation by vacancy condensation, Philosophical Magazine, 1960, 5: 43-63.

[57] J.P. Hirth, Theory of Dislocations, 2nd ed., John Wiley & Sons Inc., New York, 1982, pp. 5.

[58] E. Nes, The mechanism of repeated precipitated on dislocations, Acta Metallurgica, 1974, 22: 81-87.

[59] H. Hou, E. Simsek, T. Ma, N.S. Johnson, S. Qian, C. Cissé, D. Stasak, N.A. Hasan, L. Zhou, Y. Hwang, R. Radermacher, V.I. Levitas, M.J. Kramer, M.A. Zaeem, A.P. Stebner, R.T. Ott, J. Cui, I. Takeuchi. Fatigue-resistant high-performance elastocaloric materials via additive manufacturing. Science, 2019, 366: 1116-1121.